Fluorescence and Diffuse Reflectance Spectroscopy for Margin Analysis in Breast Cancer

Fluorescence and Diffuse Reflectance Spectroscopy for Margin Analysis in Breast Cancer

BY: NOURHAN SHALABY

A THESIS SUBMITTED TO THE SCHOOL OF GRADUATE STUDIES FOR FULFILMENT OF THE REQUIREMENTS FOR THE DEGREE MASTER OF SCIENCE

MCMASTER UNIVERSITY

INTERDISCIPLINARY GRADUATE PROGRAM IN RADIATION SCIENCES AND HEALTH AND RADIATION PHYSICS

MCMASTER UNIVERSITY

HAMILTON, ONTARIO

Title: Fluorescence and Diffuse Reflectance Spectroscopy for Margin Analysis in Breast Cancer

AUTHOR: NOURHAN SHALABY

B.SC. MEDICAL SCIENCE AND BIOLOGY

WESTERN UNIVERSITY, CANADA

SUPERVISOR: PROF. MICHAEL FARQUHARSON

CO-SUPERVISOR: DR. THOMAS FARRELL

NUMBER OF PAGES: XI, 80

Abstract

This study investigates the possibility of using a time-resolved Fluorescence and Diffuse Reflectance Spectroscopy (tr-FRS) system to define tumour surgical margins of invasive ducal carcinoma of breast. UV excitation light was used for the fluorescence component and data was collected from the 370-550 nm range. A broadband source was used for diffuse reflectance collection and the emitted response was in the 400-800 nm range. 40 matched pair cases were collected from patients undergoing breast conservation surgeries. Histological analysis was performed on each sample to determine the fat and tumour content within each normal and tumour sample respectively. Statistical analysis was performed on the optical data to reveal biochemical changes in the endogenous fluorophores collagen, reduced nicotinamide adenine dinucleotide (NADH), and flavin adenine dinucleotide (FAD) as well as changes in absorption and scattering properties attributed to variances in absorber concentrations and cell density respectively. Statistical significant differences in collagen, NADH, and FAD lifetimes, collagen, NADH, FAD and NADH/FAD intensity, diffuse reflectance and reduced scatter coefficient were observed between tumour and normal breast samples. These significant factors were used in Principle Component Analysis model construction and a binary classification scheme using Soft Independent Modeling of Class Analogy (SIMCA) was used as a classification tool to predict unknown breast samples as either normal or tumour with specificity of 60% and sensitivity slightly over 50%.

Acknowledgements

First and foremost I would like to acknowledge my supervisor Prof. Michael Farquharson for his advice and guidance throughout my masters period. I would also like to thank my co-supervisor Dr. Thomas J. Farrell for his encouragement and feedback on my work as well as my committee member Dr. Qiyin Fang for his positive guidance and assistance throughout the project. I would especially like to thank Dr. Du Le for his collaboration and assistance in data collection as well as Dr. Alia Al-Ebraheem for her guidance in data analysis. Furthermore, I would like to thank the Juravinski Hospital and Cancer Centre Foundation Fall 2014 Research Grant for providing the financial support to carry out this research. Special thanks to Dr. Peter Lovrics and Dr. Susan Reid for their collaboration on this project and providing the breast tissue used in this work. I would also like to acknowledge Dr. Gabriela Gohla for conducting histological analysis on the breast samples. Finally, I would like to thank God, my husband, parents and siblings for their positive encouragement, love and support.

Table of Contents

List of Figures

List of Tables

List of Abbreviations

AOTF: Acousto-Optic Tunable Filter

BBS: Broadband source

CF: Collection fibres

CM: Concave mirror

DM: Dichroic mirror

DOT: Diffuse Optical Tomography

DR: Diffuse Reflectance

FAD: flavin adenine dinucleotide

FWHM: full width half maximum

HWHM: half width half maximum

IDC: Invasive Ductal Carcinoma

IQR: Inter-quartile range

LPF: Long pass filter

MCP-PMT: microchannel-plate-photomultiplier tube

MF: Mirror flipper

NA: numerical aperture

NADH: Reduced nicotinamide adenine dinucleotide

NDF: Neutral density filter

OCT: Optical Coherence Tomography

OD: Optical density

PAT: Photoacoustic Tomography

PC: Principle Component

PCA: Principle Component Analysis

PCL: Plano convex lens

SIMCA: Soft Independent Modeling of Class Analogy

TRF: Time-resolved fluorescence

Tr-FRS: Time-resolved fluorescence and reflectance

UV: ultraviolet

VIP: vacuum infiltration tissue processor

GERD: Gastro-esophageal reflex disease

Chapter 1: Introduction

1.1 Motivation

According to the 2016 Breast Cancer statistics, 1 in 9 Canadian woman will be diagnosed with breast cancer and it is estimated to effect 25,000 women each year. The prevalence of breast cancer is more than 100 times lower for men, with about 220 Canadian men being diagnosed with the disease. There are many types of breast cancers including invasive, non-invasive, recurrent and metastatic breast cancer. Invasive ductal carcinoma (IDC) is the most common type accounting for about 80% of all breast cancer incidences (Statistics., 2015). This cancer type begins in the milk ducts and makes its way to invade other tissues within the breast. If untreated, IDC can spread into the lymph nodes and possible other areas of the body. This highlights the importance of early detection of the disease, as the chances of recovery improve if tumour size is small.

Breast cancer diagnosis can be as simple as a physical examination performed to see if there is any enlargement of lymph nodes or any swelling or unusual changes in the breast. Mammography is a diagnostic tool that uses low-dose x-rays to detect breast cancer in woman with reported sensitivity and specificity of around 70% and 75% respectively (Kuhl et al., 2005). The main limitation in mammography is the low accuracy of tumour detection in woman with denser breasts, as dense breasts present in a similar way to breast cancer in a mammogram. This can lead to increases in recall rates, reduces specificity and compromises screening benefits for women with denser breasts (Carney et al., 2003). The use of ultrasound as a diagnostic technique for breast cancer is also common in conjunction with mammography. Although ultrasound has a slightly higher sensitivity than mammography, the combination of both will yield a higher

sensitivity, which is still insufficient for early and accurate diagnosis of breast cancer in women (Kuhl et al., 2005). MRI can be used for diagnosis, resulting in the detection of intraductal and invasive cancer with significantly higher sensitivity (91%) than mammography and ultrasound combined (Kuhl et al., 2005).

The above screening procedures are the first step in diagnosing breast cancer (Volynskaya et al., 2008). However, these procedures do not accurately identify malignant tissue. Since these screening procedures have low specificity of tissue diagnosis, where approximately 70 to 90% of suspected lesions are found to be benign or normal, the gold standard for breast cancer diagnosis remains a tissue biopsy followed by histopathological analysis (Tadrous et al., 2003). This invasive procedure results in patient trauma, additional medical costs and time delay.

For the past couple of decades, optical techniques have been used to reduce the number of unnecessary biopsies in a minimally invasive manner. This method of using light to classify tissue is referred to as “optical biopsy” (Pu et al., 2012). Optical biopsies have been used to obtain fundamental information about the molecular level of tissues.

In this study, tissue was collected (from woman who have undergone lumpectomies and mastectomies of invasive ductal carcinoma) at two different regions in the breast; a tumour region and a further normal region was collected. Measurements were made on each excised sample with an optical spectroscopy system; the time-resolved fluorescence and reflectance (tr-FRS) system.

The (tr-FRS) system used in this study is an incorporation of two modalities in itself, with the ability to measure diffuse reflectance as well as fluorescence intensity and lifetime of tissues via a fibre optic probe that collects both measurements from the same physical

location. The diffuse reflectance component of the optical device uses a light source with a broadband UV-VIS wavelength region coupled with detection fibres at various distances from the source fibre to collect the diffuse reflectance spectra in the 400-800 nm range. Diffuse reflectance can interpret how light is back scattered or absorbed from tissue and can be used to estimate optical properties such as the absorption and reduced scattering coefficients. The absorption and reduced scatter coefficient can subsequently reveal physiological and morphological information respectively of the tissue. The absorption coefficient reveals information on tissue absorber such as oxygenated and de-oxygenated haemoglobin and beta carotene concentration and saturation while the reduced scattering coefficient reveals information on the size and density of scattering centers in tissue, such as cells and nuclei which have been shown to be significantly different between malignant and normal tissue (Zhu et al., 2006).

The time-resolved fluorescence component includes rapid data acquisition within a broad range of emission wavelengths (380 to 550 nm). Excitation light is a very short pulsed-laser that is coupled to the optical fibre and excites the tissue under examination. Thus, the fluorescence emitted from the tissue is collected using the same optical fibre and this light is coupled through filters to a fast detector. Fluorescence can be measured in two ways; time-resolved or steady state measurements. In time-resolved fluorescence, intensity and dynamic decays are measured once the sample is exposed to pulsed light which is typically shorter than the decay time of the sample. A high-speed detector will then record the intensity decay on the nano-second timescale. In steady state measurements, the sample is continuously illuminated with a beam of light and the fluorescence intensity is collected. Simply put, steady state measurement is an average of

the time-resolved fluorescence over the intensity decay of the sample and does not account for all of the molecular information reported by fluorescence (Wehry, 1984). In this device, time-resolved fluorescence in the wavelength range of 380 to 550 nm is used.

The presence of a clear surgical margin is the most important indicator available to ensure completeness of surgical excision. A positive surgical margin is a major predicator of local recurrence, independent of tumour factors and adjuvant therapies. Furthermore, the presence of positive margins generally leads to further surgical resections with associated morbidity, resource utilization, anxiety and delay. Positive margin rates for breast conserving surgery can range from 4-31%, resulting in approximately 25% of breast cancer patients requiring repeat surgery (Sun et al., 2010). The current standard relies upon permanent histopathology evaluation of margins, which are available 5 to 7 days following surgery. Current intra-operative assessments including "frozen section" or "touch-prep cytology", have been shown to decrease the need for re-operation and recurrence rates, but remain time consuming and labour intensive and are not readily transferable to routine practice.

A preliminary clinical study was carried out by our team in order to evaluate whether the tr-FRS system is capable of differentiating between tumour and normal breast tissue in both the freshly excised and pre-frozen samples. The results of this study showed the validity of using archived frozen breast tissues from a tissue bank to simulate the fluorescence response and optical properties of fresh breast tissue. Therefore we were able to conduct the current study using archived pre-frozen tissue to provide an immediate intra-operative margin assessment system by developing a mathematical model using the data retrieved from the (tr-FRS) system that can define an unknown

tissue as either malignant or normal. This (tr-FRS) system will have the advantage of being fast, quantitative, and minimally invasive, while having the potential to improve breast cancer treatments by assessing surgical margins for residual cancer in vivo during surgery.

1.2 Literature Review

For the past couple of decades, optical techniques have been used to reduce the number of unnecessary biopsies in a minimally invasive manner. A couple of common methods used in optical biopsies include single-spectroscopic techniques such as fluorescence and diffuse reflectance, which will be discussed below.

Fluorescence techniques have been widely used in cellular studies to detect biochemical composition, reactions and structures. Endogenous fluorophores have the ability to monitor cellular environments because of their proportional changes during the transition from normal to pathological conditions. Monitoring fluorescence of endogenous fluorophores can be achieved by either steady-state fluorescence spectroscopy or time-resolved fluorescence spectroscopy. Both steady state and time-resolved spectroscopy use similar instrumentation. The basic instrumentation of a spectrofluorometer are a light source, a monochromater (used to disperse polychromatic light into various wavelengths by using prisms or diffraction gratings) and a detector. Photo-multiplier tubes (PMTs) are used in almost all fluorometers as detectors to respond to individual photons as they are low-noise amplifiers for low-level light (Wehry, 1984). Typically, an excitation beam with a narrow wavelength range is used for illuminating a sample. Fluorescence emissions are collected perpendicular from excitation to prevent excitation light from interfering with the fluorescence signal. The weak fluorescence signal collected enters a

spectrograph and a detector registers the spectrum. The main difference between the instrumentation is that time-resolved uses a pulsed-light source and gated detection of the fluorescence emission. In steady-state fluorescence intensity is measured over a broadband spectral region while in time resolved, the fluorescence intensity as well as dynamic fluorescence decay is measured to obtain fluorescence lifetime. Time-resolved is more advantageous as fluorescence lifetime is independent of emission and can be used to differentiate between various fluorophores with overlapping emission spectra. Much of the time-averaging process in steady state measurements eliminates valuable molecular information such as the precise shape of the anisotropy decay, which relays information on molecular shape and flexibility. Therefore, time-resolved fluorescence spectroscopy delivers additional information compared to steady-state fluorescence techniques (Wehry, 1984).

In 1981, Alfano was first to use light to detect and diagnose teeth decay. He later used this approach to illuminate cancerous and normal rat kidney, prostate and bladder tissue using an Argon laser with a 488nm excitation beam to reveal that malignant and normal tissue have substantially different fluorescence spectra (Alfano et al., 1984). In 1987, he continued his work with steady-state fluorescence on malignant and normal human breast and lung tissue and used two excitation wavelengths of 488nm and 458 nm. Alfano's work confirmed a difference in emission characteristics between normal and malignant tissues and attributed these differences to endogenous fluorophores within the cell that fluoresce in specific spectral regions, providing information about the microenvironment of pH, redox potential, bonding sites, polarity and ion concentration (Alfano et al., 1987). Since then, several groups continued to investigate fluorescence spectroscopy of ex vivo

malignant and normal breast tissue (Yang et al., 1997, Gupta et al., 1997, Alfano et al., 1987, Ghosh et al., 2001). Gupta et al (1997) used excitation wavelengths of 340 and 488 nm on ex vivo breast tissue to exhibit significant differences in emission spectra at 390 and 460 nm with a sensitivity and specificity of 98%, which he attributed to NADH and Collagen (Gupta et al., 1997). Yang et al, (1997) used 300 nm excitation to produce 340 nm emission spectra, where tryptophan is the main fluorophores, to separate tumor from normal tissue with 93% sensitivity and 95% specificity rates (Yang et al., 1997). He found that the fluorescence emission peak at 340 nm was red-shifted for malignant samples relative to that of normal adipose tissues and the fluorescence at around 450-nm emission was decreased in malignant relative to fibrous tissue. Despite these promising results, these studies had one main limitation; data collection time of 2 – 3 minutes (Mourant et al., 1995)). Another limitation was the use of one or several wavelength to obtain fluorescence spectra. In addition, the several hundred micrometers of penetration depth of the UV light can only read changes on the surface of the tissue, and cannot give information on depth. Another limitation is that the algorithms used were not tested to classify unknown tissue malignancy status and thus were biased.

In addition to single point spectroscopy, FLIM (fluorescence lifetime imaging) has been used to measure lifetime in clinical applications over a region of interest. Wide-field-based FLIM uses thousands of optical fibers and a detector in a fiber bundle. This technique uses a gated image detector which has low sensitivity and long data acquisition times (Requejo-Isidro et al., 2004). Scanning-based FLIM collects fluorescence decay at each pixel by scanning a beam over the tissue and a photo-multiplier tube (PMT), which has lower acquisition times in comparison to the gated image detector is used (Shrestha et

al., 2010). Multiple band pass filters have been previously used to retrieve fluorescence spectra at specific wavelengths to improve temporal resolution but this results in limited fluorescence spectra. In 2007, De Beule et al. designed a hyperspectral FLIM system with a PMT that contained 16 channels, where each channel collected fluorescence spectra, to reduce collection times (De Beule et al., 2007). To date, there are PMTs commercially available with up to 64 channels. This design however, is still relatively time consuming and takes about 45 seconds per measurement at each wavelength. Yuan et al (Yuan et al., 2009) used an Acousto-Optic Tunable Filter to collect dynamic fluorescence decay. The AOTF has the ability to switch diffracted wavelengths at a broad spectral range within the microsecond timescale. This is achieved by the AOTF's ability of applying different acoustic frequencies on a crystal to filter light during the measurement. Since switching between wavelengths can be completed in 20 μs, the fluorescence decay in the wavelength range can be collected rapidly in comparison to the previous time-resolved fluorescence systems (PMTs).

The diffuse reflectance spectrum reflects the absorption and scattering properties of the tissue. The absorption coefficient is directly related to the concentration of physiologically relevant absorbers in the tissue, which include oxygenated and deoxygenated hemoglobin and beta-carotene. The reduced scattering coefficient reflects the size and density of scattering centers in tissue, such as cells and nuclei. Instrumentation for diffuse reflectance requires a light source, a beam splitter (to split the incident light into a reference beam and an excitation beam), and spectrometers. Several studies used diffuse reflectance spectroscopy as a minimally invasive method to optically differentiate between normal and pathological tissue (Bigio et al., 2000) (Mourant et al.,

1996) (Mourant et al., 1995). Bigio et al. collected diffuse reflectance spectra mediated by a fiber optic probe through a core biopsy needle to distinguish differences between in-vivo and ex-vivo tissue types with a sensitivity of 60%–70% and a specificity of 85%–95%. The probe incorporated two optical fibers and was designed to come in physical contact with the tissue. The first optical fiber had a core diameter of 400 μm and illuminated the tissue within the range of 330-750nm. 350 μm away, lies the second parallel fiber with a core diameter for 200 μm collects the scattered light from the tissue and sends light to the spectrometer to generate the optical spectra in less than 1 second (Bigio et al., 2000). Zhu et al. (2006) worked with a different geometry for the optical probe with a central illumination fiber surrounded by three concentric rings of collection fibers with diameters of 200 μm. Only the diffuse reflectance spectra from most inner ring of fibers were analyzed as they provided the highest intensity. Spectra collection time was improved to 0.025 seconds (Zhu et al., 2006a). The changes in the diffuse reflectance of malignant tissues, was attributed to increased DNA, protein and hemoglobin absorption and increased scattering.

Endogenous fluorophores with the most significant diagnostic importance are excited in the 300-800 nm range. Fluorescence spectra recorded from these fluorophores are distorted by absorption and scattering, thus limiting the accuracy of the fluorescence spectra generated. Since diffuse reflectance has the ability to estimate the absorption and scattering coefficients of the tissue, incorporation of diffuse reflectance with fluorescence spectroscopy was used by several studies (Volynskaya et al., 2008, Palmer et al., 2003) to retrieve more accurate fluorescence spectra. This process is called Intrinsic Fluorescence spectroscopy (IFS). Palmer et al (Palmer et al., 2003), combined fluorescence with diffuse

reflectance using excitation wavelengths of 300-460 nm and revealed that only 4 wavelengths (300, 400, 420, 460) were necessary for tissue classification. This is clinically beneficial as it decreases data acquisition times and equipment costs as less complex instruments can be used to measure fewer wavelengths. Volynskaya et al, used the combination of diffuse reflectance and autofluorescence techniques to overcome the limitations of fluorescence, using a technique called Diffuse Optical Tomography (DOT) (Volynskaya et al., 2008) and obtained sensitivity and specificity of 100 and 96 respectively. In DOT, light with near-IR wavelength illuminates the tissue and contrast, provided by absorption and scattering, measures concentration of oxygenated and deoxygenated hemoglobin content. However, this technique has low resolution where small lesions (<4mm) go undetected. The DRS spectra in this study were analyzed using a mathematical model based on the diffusion approximation of light propagation in tissue to determine the values of the absorption and reduced scattering coefficient. The main advantage to the diffuse reflectance technique is that output signals are several orders of magnitude greater than weak fluorescence signals. However, diffuse reflectance was not able to differentiate between malignant and normal tissue with the same accuracy as fluorescence spectroscopy alone or the combined technique (Palmer et al., 2003). Therefore, it is advantageous to use fluorescence combined with diffuse reflectance due to the additional chemical information that arises from the fluorescence of the biological fluorophores intrinsically present in tissue.

Even though a distinction between tumour and normal tissue can be made by each of the modalities, neither can be used as a diagnostic tool on its own. The use of optical spectroscopy has been used in previous studies to achieve accurate and desirable

performance for clinical applications. However, no previous studies have incorporated optical data mapped to accurate histological analysis taking into account full chart review of patient history. Thus, our work will aim to combine the aforementioned parameters collected by the optical device in a mathematical model to achieve classification of an unknown tissue as either pathological or healthy which can have future clinical and surgical applications.

1.3 Dissertation Organization

The first chapter of this dissertation discusses the motivation of this project, the literature review for optical spectroscopy and the limitations for previous technologies. This chapter also introduces the aim and novelty of our work. Chapter 2 reviews different optical biopsies used in the diagnosis of breast cancer. The theory of fluorescence and diffuse reflectance spectroscopy is discussed in detail. Chapter 3 discusses the design of the optical fluorescence and reflectance spectroscopy (tr-FRS) system as well as examines the methodology of the study including the clinical procedure, sample preparation and handling, as well as an organized presentation of sample information. In chapter 4 a sub study is conducted where ten matched pair cases are measured directly after excision and after being frozen and thawed. This study was conducted to validate the use of pre-frozen tissue instead of fresh tissue. Chapter 5 reveals the results for the fluorescence and diffuse reflectance for the 40 matched pairs of breast tissue are presented. Histological analysis of tissue is correlated with the mathematical models for a more accurate classification of tissue. Different PCA models are examined and the use of the models to classify unknown tissue types is performed using SIMCA. Chapter 6

discusses and compares previous literature with findings from our study, concludes the research and the significance of the work presented as well as discusses future direction.

Chapter 2: Background on Optical Biopsies Used in Breast Cancer

In the last twenty years, there has been an increased focus to differentiate between pathological and healthy tissue using non-invasive techniques. However, the gold standard for breast cancer diagnosis remains a tissue biopsy followed by histological analysis. This method is invasive, time consuming and results in patient trauma. Optical biopsy is the use of light in different regions of the electromagnetic spectrum (visible, ultra-violet or infrared light) to illuminate a tissue sample and reveal pathological and morphological properties to potentially replace the current gold standard. Optical biopsies have been widely studied to differentiate between healthy and malignant tissue. Optical techniques including Raman spectroscopy, diffuse optical tomography, optical coherence tomography (OCT), photoacoustic tomography (PAT), as well as the limitations imposed by these techniques will be briefly discussed in the next section, followed by a detailed description of fluorescence spectroscopy and diffuse reflectance spectroscopy.

2.1. Raman Spectroscopy

The main use of Raman spectroscopy is determining the chemical component of a sample. Raman spectroscopy results in fingerprint spectra for each molecule based on shifted frequencies of emitted photons from a sample. When monochromatic light shines on tissue, the light reflected back from the sample is shifted in frequency, corresponding to the vibrational energy levels of the sample. In other words, upon tissue excitation with a laser light, the molecule is excited from the ground state to a virtual state. Relaxation from the virtual state to a vibrational state that is either below or above the ground state will occur, emitting a photon in the process. Raman stokes scattering is when the emitted photon has lower energy, or a longer wavelength than the incident photon whereas in

Raman anti-stokes scattering, the emitted photon has higher energy and shorter wavelength than the incident photon.

Raman spectroscopy has been used by several studies (Haka et al., 2005, Kong et al., 2015, Zhou et al., 2014) to differentiate between tumour and normal tissue based on chemical composition of biological molecules within tissue with sensitivity and specificity as high as 94% and 96% respectively.

One of the main limitations of Raman spectroscopy is the relatively low efficiency of the inelastic light scattering compared to elastic scattering. This inefficient signal to noise ratio limits the speed of the technique and can decrease accuracy when spectra are required, compromising the ability to translate the technique into clinical settings (Kong et al., 2015).

2.2 Diffuse Optical Tomography

DOT uses near-infrared (NIR) light to assess optical properties of tissue. Light absorption in the wavelength range of ~700 to 1,000 nm is minimal, allowing for sufficient tissue penetration (up to 15 cm) in breast imaging (van de Ven et al., 2009). The technique derives unique functional/physiological information such as oxy- and deoxyhemoglobins, water and lipid concentrations, tissue scattering and blood flow. Since increased angiogenesis and a change in the oxy- and deoxyhemoglobin ratio as well as a change in chromophore concentrations are features of malignant tumours, DOT can be used complementary to other imaging modalities, such as ultrasound, X-ray mammography, and magnetic resonance imaging (MRI) to assist in differentiating between normal and tumour breast tissue (Choe and Ieee, 2009). It is not a stand-alone technique since

photons undergo multiple random scattering events as they propagate through the highly scattering tissue, causing spatial information and imaging resolution to be lost. Although DOT can localize relatively large (~1 cm) tumours deep in breast tissue, poor resolutions on the order of several millimetres does not permit imaging of small early-stage tumours and cellular-level resolution is not possible (Boppart et al., 2004).

2.3 Optical Coherence Tomography (OCT)

OCT is a high-resolution imaging technique that has been used by several studies to intraoperatively detect tumour margins in rat mammary models (Iftimia et al., 2011, Nguyen et al., 2009, Boppart et al., 2004). OCT performs analogous to ultrasound except for reflection of near infrared radiation as opposed to sound waves are detected. In OCT a sample is exposed to low coherence NIR light and the back scatter is detected using a coherence gates scheme that allows for depth wise spatial mapping. The reflected light is incident upon a photodetector which converts the photons into electrical signal to be stored and analysed (Zysk and Boppart, 2006). Although imaging resolution in OCT has been measured to be as fine as 1 micron, depth of imaging is limited to only a few millimetres in highly-scattering tissue and penetration of OCT remains a limitation (Boppart et al., 2004).

2.4. Photoacoustic Tomography

Recent studies have used photoacoustic tomography (PAT) to differentiate between tumour and healthy breast tissue using the high contrast of hemoglobin to light (Heijblom et al., 2015, Li et al., 2015). Since increased vasculature is a feature of diseased state, PAT can be used as a promising diagnostic tool in breast cancer detection. The method is based on using thermoelastic expansion to convert electromagnetic energy into acoustic

pressure waves. In other words, when a tissue is irradiated with pulsed laser light, the photon energy is converted by tissue absorbers into heat and generates a rise in temperature. This rapid thermoelastic expansion results in the generation of ultrasound waves. An ultrasound transducer can detect the pressure waves generated by tissue absorbers, such as hemoglobin and melanin, and an image can be formed with the primary contrast related to the optical absorption of tissue (Mohammad Mehrmohammadi 2013). A limitation for PAT is the strong reflection of ultrasounds between two different interfaces due to a mismatch in acoustic imdepedance. Therefore high-resolution detection requires direct contact of the transducer to the biological tissue.

2.5 Fluorescence Spectroscopy

Fluorescence techniques have been extensively used in cellular studies to detect biochemical composition, reactions and structures. Endogenous fluorophores have the ability to monitor cellular environments because of their proportional changes during the transition from normal to pathological conditions.

When a biological molecule is illuminated with a wavelength that matches its absorption spectrum, it will be elevated from ground state (S0) to excited state (S_1 or S_2). The molecule can return to ground state either radioactively or non- radioactively. Non-radiative processes of relaxation include vibrational relaxation and internal conversion. Radiative processes include fluorescence emission, where the molecule will releases its energy and returns back to ground state. This process occurs in a nanosecond time scale. The emitted spectrum of the fluorophore is red-shifted from the excited spectrum. Another parameter that characterizes the fluorescence phenomenon of the molecule is fluorescence lifetime. Fluorescence lifetime is the average time a biological molecule

takes to return to ground state from an excited state. The fluorescence decay of a single fluorescent molecule (fluorophore) can be described as the exponential function below;

$$I = I_0 \exp(-t/\tau)$$

where I_0 is the initial intensity at time 0 and τ is fluorescence lifetime, calculated from the time it takes the intensity to decrease to 1/e of the peak intensity. The decay of multiple fluorophores can be presented as the sum of the exponential components of each fluorophore:

$$I(t) = \sum_{i=0}^{N} I_{0_i} \exp(-t/\tau_i), i = 1...N$$

where i represents the i^{th} fluorescence component. The average lifetime can then be calculated as;

$$\tau_{avg} = \frac{\left(T \cdot \sum_{n=0}^{k} k \cdot h(k)\right)}{\sum_{n=0}^{k} h(k)}$$

where k is the data length of the decay curve, T is the sampling time interval and h(k) is the intrinsic fluorescence decay (Nie et al., 2016). Fluorescence has been widely studied in biological tissue to monitor changes in the cellular level. Both endogenous and exogenous fluorescence have been used. This work will focus on endogenous fluorescence in biological tissue. Endogenous fluorophores include amino acids (tyrosine, phenylalanine and tryptophan), structural proteins (collagen and elastin) and enzyme co-factors NADH and FAD can reveal information about cellular environments, such as biochemical composition, cellular structure, red-ox state and cellular metabolic states. This information can be beneficial when classifying tissue as malignant, or healthy since

tumour states display different cellular environments and metabolic states. For example, NADH concentration is found to be higher in cells with higher metabolism. Since NAD+ is non fluorescence when excited by a UV laser, and only the reduced counterpart NADH will fluorescence in the 450-460 nm range, the NADH emission can serve as an aid in tumour detection. Furthermore, NADH displays a short and long lifetime depending on the protein-binding status of the coenzyme. This is also beneficial since malignant tissue display an altered ratio of bound to free NADH. Figure 1 below shows the different fluorescence emission spectra of various molecules within the body after being excited with a 366 nm light source.

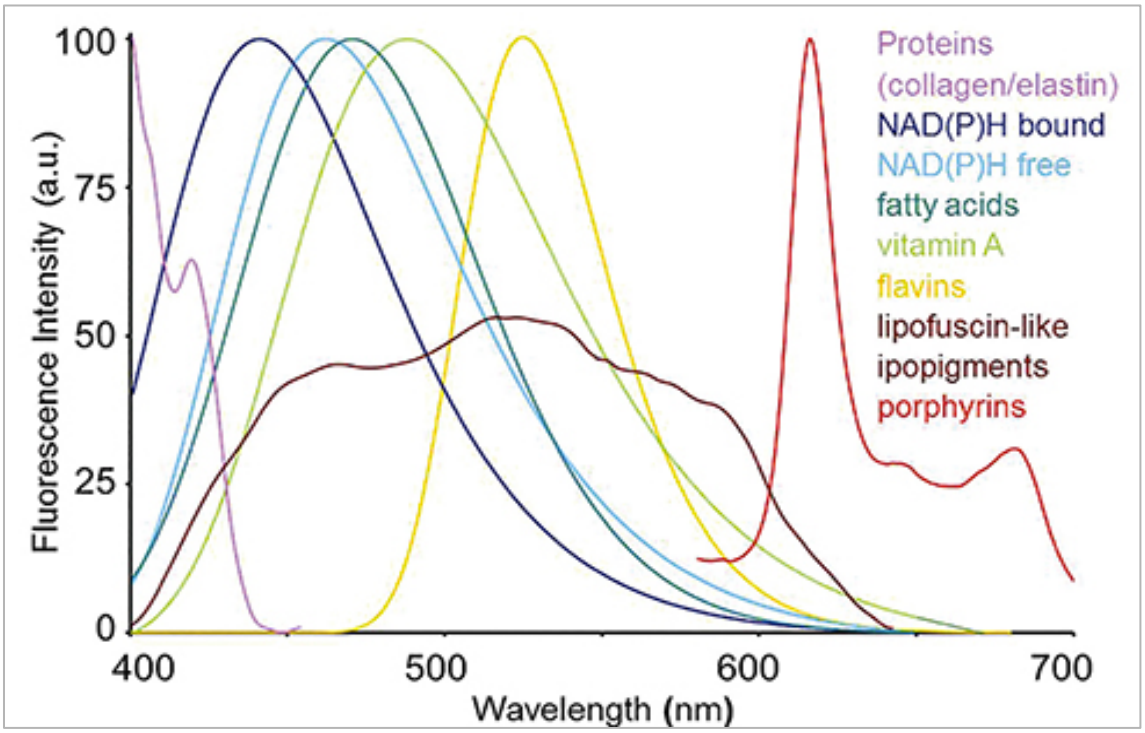

Figure 1: Typical spectral response of autofluorescence emission from single endogenous fluorophores from 400-700 nm (Croce and Bottiroli, 2014) with an excitation light of 366 nm. Spectra were normalized to the maximum emission peak for presentation.

Table 1 below summarizes some of the endogenous fluorophores present in breast tissue, their excited and emitted wavelength as well as lifetime (Ramanujam, 2000, Chorvat and Chorvatova, 2009).

Endogenous Fluorophore	Excited wavelength (nm)	Emitted wavelength (nm)	Lifetime (ns)
Collagen	325, 360	390, 415	2.46-3
NADH (free state and protein-bound)	290, 351	440, 460	0.4-3.4
FAD, flavins	450	535	2.3-5

Table 1: The excited and emitted wavelength, and lifetime of collagen, NADH, and FAD (Ramanujam, 2000, Chorvat and Chorvatova, 2009).

Monitoring fluorescence of endogenous fluorophores can be achieved by either steady-state fluorescence spectroscopy or time-resolved fluorescence spectroscopy. Both steady state and time-resolved spectroscopy use similar instrumentation. The basic instrumentation of a spectrofluorometer are a light source, a monochromater and a detector. The monochromater is used to disperse polychromatic light into various wavelengths by using prisms or diffraction gratings. Photo-multiplier tubes (PMTs) are used in almost all fluorometers as detectors to respond to individual photons as they are low-noise amplifiers for low-level light (Wehry, 1984). Typically, an excitation beam with a narrow wavelength range is used for illuminating a sample. Fluorescence emissions are collected perpendicular from excitation to prevent excitation light from interfering with the fluorescence signal. The weak fluorescence signal collected enters a spectrograph and a detector registers the spectrum. The main difference between the instrumentation is that time-resolved uses a pulsed-light source and gated detection of the fluorescence emission. In steady-state, fluorescence intensity is measured over a

broadband spectral region while in time resolved, fluorescence intensity as well as dynamic fluorescence decay is measured to obtain fluorescence lifetime. Time-resolved is more advantageous as fluorescence lifetime is independent of emission and can be used to differentiate between various fluorophores with overlapped emission spectra. Much of the time-averaging process in steady state measurements eliminates valuable molecular information such as the precise shape of the anisotropy decay, which relays information on molecular shape and flexibility. The intensity decays measured in steady state also contain information that is lost in the averaging process. Therefore, time-resolved fluorescence spectroscopy delivers additional information compared to steady-state fluorescence techniques (Wehry, 1984).

A limitation for time resolved fluorescence (TRF) technique is the penetration depth of the excitation light. A UV light has an excitation source typically has a penetration depth of several hundred micrometers. As a result, only the surface of the tissue is measured using the TRF and no depth information that is necessary for surgical resection can be provided. Another limitation is the alteration of the light passing through the tissue and being effected by absorption and scattering of tissue and blood. This suggests that the fluorescence signal may not reflect its real fluorescence properties. This problem is conquered by integrating a method known as diffuse reflectance, which can reveal optical properties that can adjust the fluorescence intensity into a more accurate intrinsic fluorescence of the fluorophores (Volynskaya et al., 2008, Zhu et al., 2008).

2.6 Diffuse reflectance Spectroscopy and Optical Properties

In diffuse reflectance, a broadband light is used to excite tissue using an optical fibre probe. Multiple absorption and scattering events will take place and light will be

transmitted in different directions. The probe will collect the diffuse reflected light coming from the tissue, near the original illuminated location. DRS is used to resolve optical properties of biological tissue. The optical properties of tissue can be extracted from the diffuse reflectance spectra using diffuse theory or Monte Carlo simulations (Cappon et al., 2013). The optical properties recovered include the absorption coefficient, μ_a, and reduced scatter coefficient, μ_s'.

When light illuminates tissue, the light will be either scattered or absorbed by the tissue. Scattering and absorption events can provide information on tissue heterogeneity. Scattering events occur as a result of scattering centers in the cell such as nuclei and provide information on molecular size and the structure of tissue. Absorption events can relay information on the concentration of absorbers (oxygenated hemoglobin, deoxygenated hemoglobin) which is important for cancer diagnosis since increased angiogenesis is common in cancer cells. The scattering phenomenon is a result of a mismatch of the refractive index. The scattering coefficient, (μ_s) is the probability of a scattering event per unit distance. There is an angular dependence of scattering distribution between the directions of incident and scattered light. This angular dependence can be explained by the anisotropy factor,

$$g = \int_{-1}^{1} \cos\theta \cdot f(\cos\theta) \cdot d(\cos\theta)$$

where forward and back scatter are represented by g=1 and -1 respectively (Jacques, 2013) and characterizes tissue scattering in terms of the relative forward versus backward direction of scatter.

The reduced scattering coefficient, (μ_s') and absorption coefficient properties describe diffusion of light in a tissue and reflection of scattered light from biological tissue. These optical properties govern the reflectance from a tissue seen by a camera or the lateral diffusion of light within a tissue collected by an optical fiber probe. The reduced scattering coefficient, (μ_s') can be calculated as:

$$\mu_s' = \mu_s(1 - g)$$

The absorption coefficient, (μ_a) can be calculated as the inverse of the distances between two absorption events. The main absorbers in biological tissue include chromophore, oxygenated and deoxygenated hemoglobin, carotenes and melanin (Jacques, 2013). The optical window refers to the region between 800-1100 nm where low absorption takes place. The absorption coefficient, μ_a (cm^{-1}) is defined as :

$$\mu_a = -\frac{1}{T}\frac{\partial T}{\partial L}$$

where T (dimensionless) is the transmitted or surviving fraction of the incident light after an incremental path-length ∂L (cm). This fractional change ∂T/T per ∂L yields an exponential decrease in the intensity of the light as a function of increasing path length L(Jacques, 2013).

Chapter 3: Methodology: Integrated time-resolved fluorescence and diffuse reflectance spectroscopy system

The TRF spectroscopy measures fluorescence intensity and lifetime of fluorophores, providing information on biological composition of tissue (Berezin and Achilefu, 2010, Nie et al., 2013, Chorvat and Chorvatova, 2009). DRS reveal optical properties that relay information on absorber concentration as well as scattering size, structure and density of cells (Zhu et al., 2006a, Jayanthi et al., 2012, Glennie et al., 2014). Although both techniques have been used separately to classify tissue types, the integration of both modalities allows the yield of higher sensitivity and specificity then each modality alone. Figure 2 shows the integration of the two subsystems.

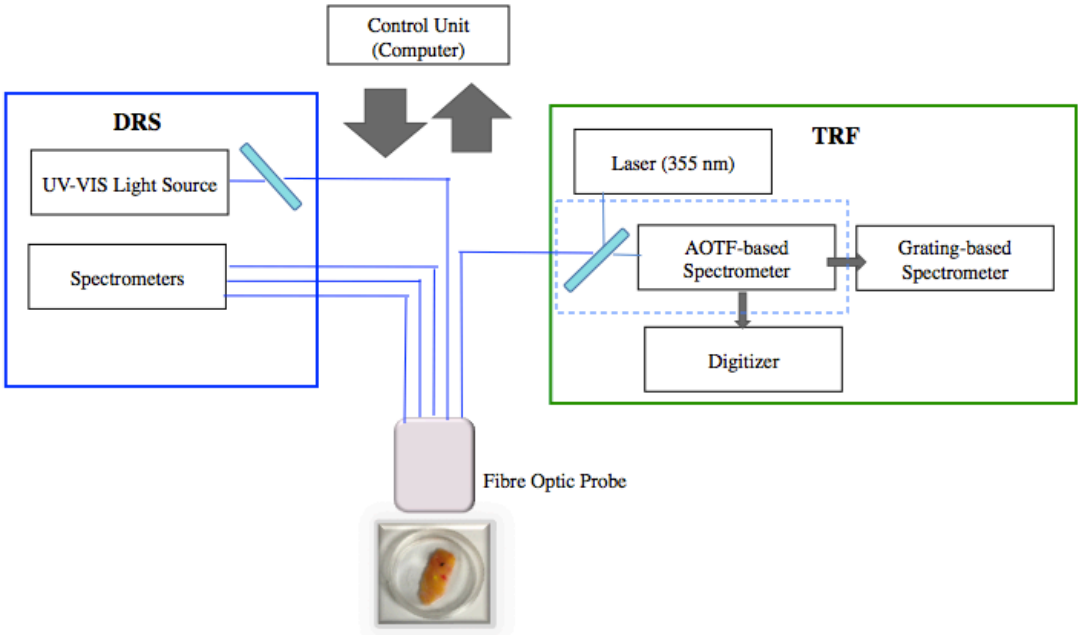

Figure 2: An illustration of the integration of the DRS subsystem (left) and the TRF subsystem (right) with data collection occurring through a probe and a central control unit (computer).

3.1 TRF Spectroscopy System

The TRF subsystem uses a UV laser Nd:YAG laser (PNV-001525-140, Teem Photonics, Meylan, France) source of 355 nm with a pulse width of 300 picoseconds (full width half maximum) and a repetition rate of 1kHz. Although the laser energy is 30 μJ, the tip of the laser is adjustable and only about 3 μJ is required for biological tissue to avoid photobleaching. After the light is attenuated by a neutral density filter [optical density (OD):0.3, ND03A, Thorlabs, NJ], it is reflected off a dichroic mirror (CS0238, Lightwaves 2020 Inc, Milpitas, CA) with 70% reflection at 45° where a plano convex lens (LA1951-A, Thorlabs, Newton, NJ) will focus the laser into an optical fibre with core diameter of 400 μm and numerical aperture (NA) of 0.12. As shown in figure 3, once the laser light illuminates the tissue, the emitted fluorescence is received by the same optical fiber. The plano-convex lens then collimates the fluorescence to a 6mm beam and an aperture with 6mm diameter following the lens prevents dispersed fluorescence. The fluorescence travels through a dichroic mirror that allows for 90% transmission and a long-pass filter (OD > 6 at 355 nm LP02-355RU-25, Semrock, Rochester, NY) that prevents backscatter of fluorescence. The fluorescence will then be transmitted through the Acousto-optic tunable filter (AOTF) where multiple events will occur. The fluorescence is separated into ordinary polarized, extra ordinary polarized and undiffracted light. The diffracted light will diffract towards two concave mirrors, while the undiffracted light passes will hit a beam stop. The AOTF switches between wavelengths in less than 20 μs and allows for rapid collection of fluorescence in the range of 370-550 nm upon a change in acoustic frequency. The diffracted beams are then collected by a fast-gated microchannel-plate-photomultiplier tube (MCP-PMT R5916-50,

rise time: 180 ps, Hamamatsu Photonics, Japan). A preamplifier (gain: 63 dBm, bandwidth: 50 KHz-1.5 GHz, C5594-12, Hamamatsu Photonics, Japan) amplifies the signal from the MCP-PMT and a high speed digitizer (ADQ412, 12 bit, 3.6 GS/s, 1.3 GHz bandwidth, SP Devices, Sweden) digitizes the signal. A photodiode (jitter of ~100 ps, DET10A, Thorlabs, Newton, NJ) collects the laser light reflected by the neutral density filter and triggers the digitizer. A pulse generator (QC9512, Quantum Composer, Bozeman, MT) is used to allow synchronization of the laser with the MCP-PMT. This allows the fluorescence decay to be collected within the gating window of the PMT.

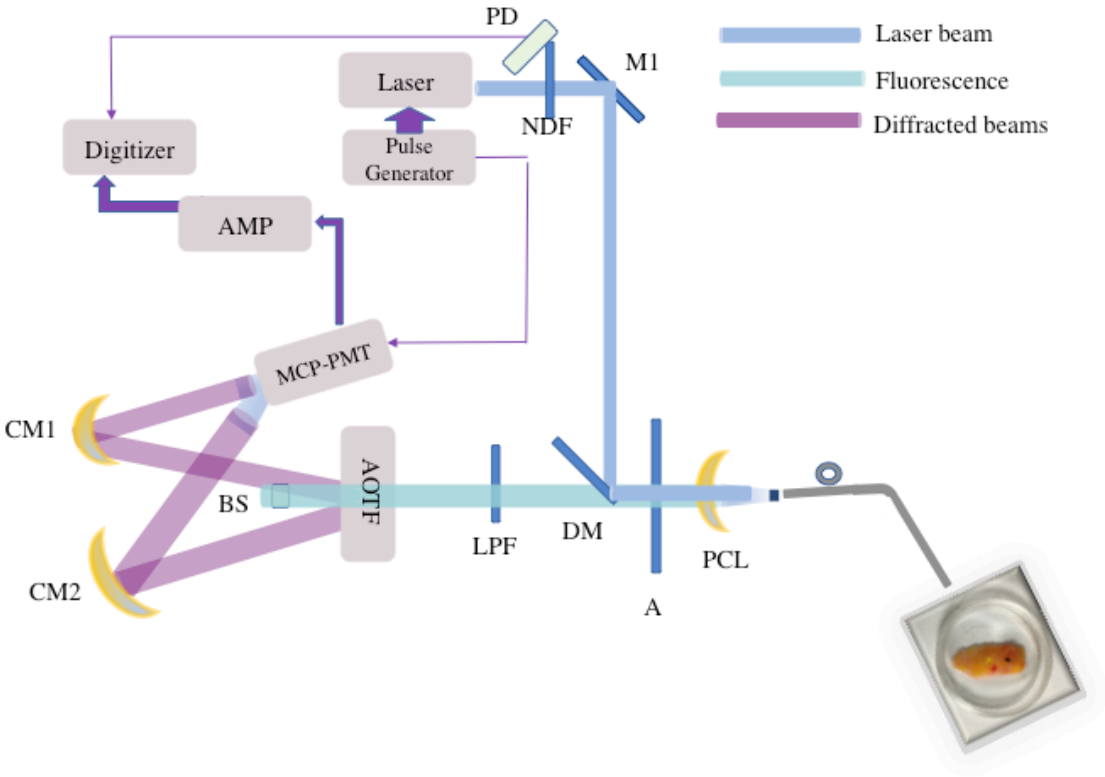

Figure 3: Collection of time-resolved fluorescence decay. M1: Mirror; PD: Photodiode; NDF: Neutral density filter; DM: Dichroic mirror; A: Aperture; PCL: Plano-convex lens; LPF: Long pass filter; BS: Beam stop; CM1: Concave mirror 1; CM2: Concave mirror 2

After the collection of fluorescence decay, the set up of the spectrometer is changed, as shown in figure 4 below to a non-diffracted wavelength to allow for collection of steady

state fluorescence. This results in light passing through the AOTF without any diffracted beam. A mirror sitting on a mirror flipper is placed after the AOTF and when in the vertical position, reflects the fluorescence beam into a grating-based spectrometer to allow for the collection of fluorescence spectra. The pulse generator flips the mirror to switch between the different modes of data collection.

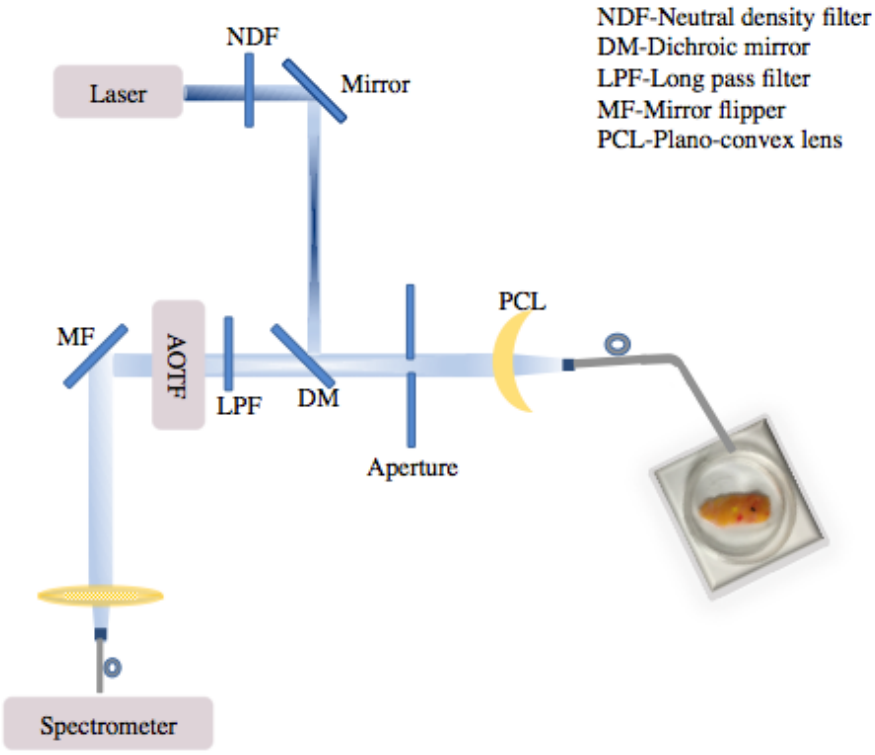

Figure 4: Steady-state collection of fluorescence. NDF: Neutral density filter; DM: Dichroic mirror; A: Aperture; PCL: Plano-convex lens; LPF: Long pass filter; MF: Mirror flipper.

3.2 DR Spectroscopy System

As shown in figure 5, the excitation source in the DRS subsystem consists of 3 UV LED lights (370 nm, 385 nm, and 400 nm, Lumibright, Innovation Optics, Woburn, MA) and a 150 W tungsten-halogen lamp (MI-150, Edmund Optics, Barrington, NJ) combined and collimated by a light coupler to ensure homogenous light. This output light is combined

into a beam of 425 nm by a dichroic mirror (DLMP425, Thorlabs, NJ). This light passes through a 20/80 beam splitter (FOS-400-0102-80/20-123, Fibersense and Signals, San Jose, CA) where light is divided 20% as a reference beam and 80% will be used on the sample using a 200 µm core optical fibre. A shutter is placed before the optical fiber coupler to control the light. Diffuse reflectance is collected at three different detector-source distances. Four spectrometers are used to individually collect the light at the reference channel as well as at each of the distances. DR measurements were conducted in the dark and background noise was also accounted for and subtracted from the measured DR spectra using the following equation:

$$R(\lambda) = \frac{(I_M(\lambda) - I_{BG}(\lambda))}{(I_{REF}(\lambda) - I_{BG}(\lambda))}$$

where R is the measured diffuse reflectance, I_{BG} is the background noise and I_{REF} is the intensity from the calibrated reference beam and I_M is the measured diffuse reflectance of the sample. The spectra are normalized to the reference light to account for variations of intensity.

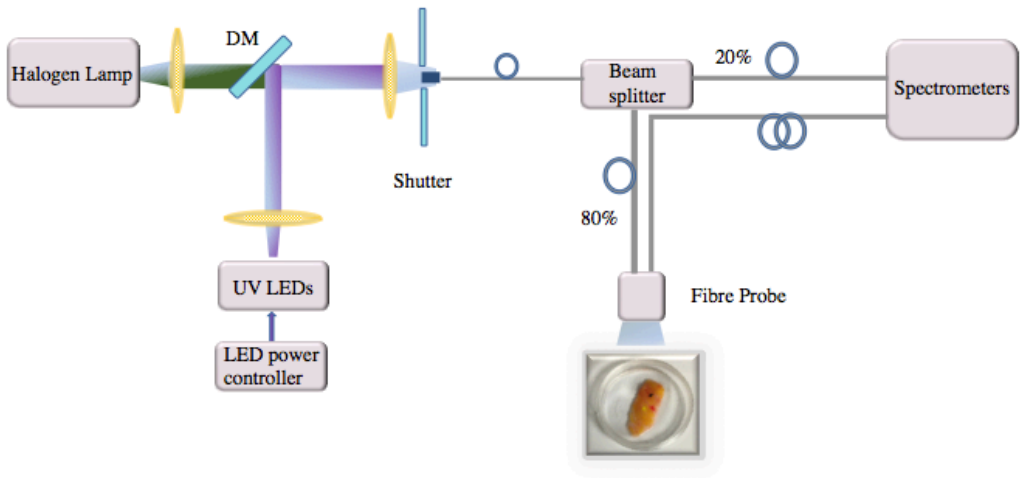

Figure 5: The DRS subsystem components with a broadband source combination of a halogen lamp and 3 UV LEDs, a beam splitter and spectrometers.

3.3 Fiber Optic Probe

The fiber optic probe shown in figure 6 and 7 allows for the integration of the TRF and DRS system to collect both fluorescence and diffuse reflectance. The diameter of the probe is 2 mm, which makes it suitable to be used as a hand-held surgical device. The probe's core has an optical fiber with diameter of 400 μm and NA of 0.12, which is used for laser excitation in the TRF subsystem. Another optical fiber with a 200 μm diameter and an NA of 0.22 is placed on the side of the probe, used for the broadband excitation source of the DRS subsystem. Bundles of fibers, with diameter of 0.23 mm, are arranged at three different distances (0.23 mm, 0.59 mm, and 1.67 mm) from the optical fibre on the side of the probe. This arrangement has been designed using Monte Carlo simulations and allows for the extraction of the optical properties and this probe set up to allow for better sensitivity in comparison to other probe geometries (Papaioannou et al., 2004, Cappon et al., 2013).

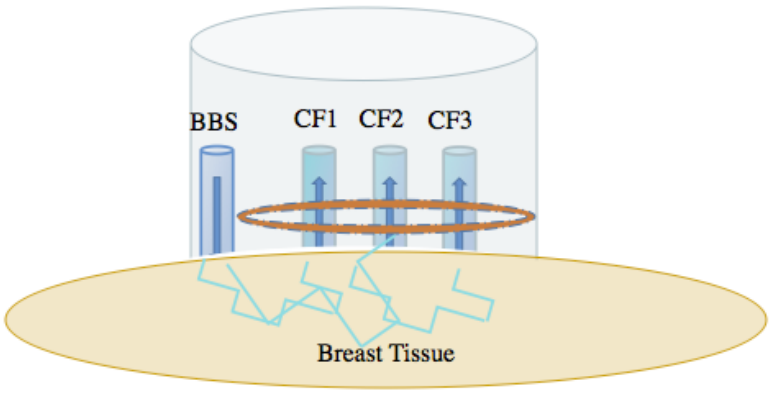

Figure 6: BBS: Broadband source; CF: Collection fibres

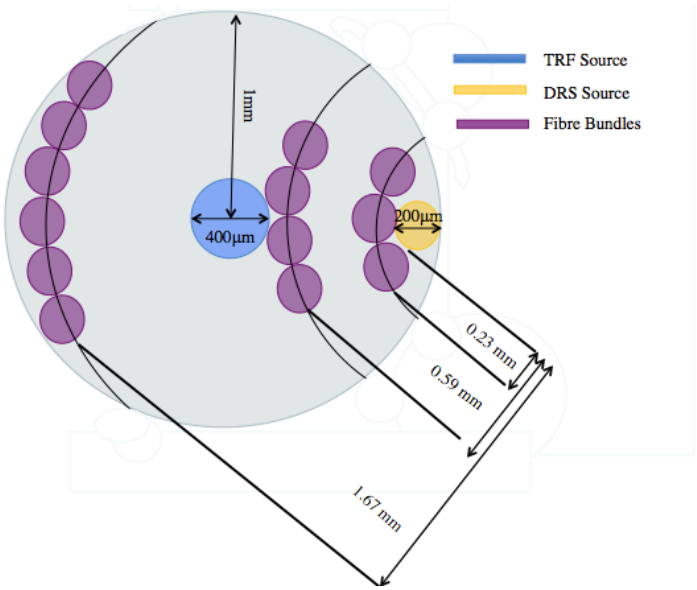

Figure 7: Transverse view of fibre optic probe. All fibres are 0.23 mm, unless indicated otherwise.

3.4 Sample Information

Table 2 summarizes the fifty breast samples collected in this study in accordance to their age, menopausal status, smoking status, tumour type, tumour grade, type of surgery, Estrogen receptor status, progesterone receptor status, Her2neu status, chemotherapy status and co-morbidities.

	Selection	Prevalence	Percentages (%)
Age (Range 32-90)	30's	1	2
	40's	9	18
	50's	13	26
	60's	13	26
	70's	7	14
	80's	6	12
	90's	1	2
Menopausal Status	Pre-menopausal	12	24
	Peri-menopausal	1	2
	Post-menopausal	37	74

Smoking Status	Non-Smoker Pre-Smoker Smoker	34 3 13	68 6 26
Tumour Type	Ductal Lobular Mix Lobular and Ductal	44 4 2	88 8 4
Tumour Grade	1 2 3 4	3 22 10 18	6 44 20 36
Type of Surgery	BCS Mastectomy	29 21	58 42
Estrogen Receptor status	Non-present Present	10 40	20 80
Progesterone Receptor status	Non-present Present	17 33	34 66
Her2neu status	Non-present Present	40 10	80 20
Chemotherapy	No Yes	50 0	100 0
Co-morbidities	No Yes	12 38	24 76

Table 2: A summary of patient information including age range, menopausal status, smoking status, tumour type, tumour grade, type of surgery, Estrogen receptor status, Progesterone receptor status, Her2neu status, use of chemotherapy and co-morbidities.

Out of the 50 matched pair specimens, over 50% of the women were in the 50-60 age range. Only one patient was in their 30's and one patient in their 90's, skewing the range wider for the data set. 74% of the women from the study were in post-menopausal status, which could indicate correlation with disease prevalence. Most of the women from the

study are non-smokers. Invasive Ductal Carcinoma accounted for 88% of the breast cancers in the total samples, while 4% showed a mixture of lobular and ductal tumour cells. Tumour grades 2 and 4 had the highest occurrence with prevalence of 44% and 36% respectively amongst the 50 women. The surgery types were either mastectomies or BCS and the prevalence of each is about half. The presence of the Estrogen receptor occurred in 4 out of 5 women while the progesterone receptor was present in about 2/3 of the women. No patients had undergone chemotherapy and 76% of the women had co-morbidities. Co-morbidities include hypertension, osteoarthritis, hypercholesterolemia, diabetes, obesity, osteoporosis, gastroesophageal reflex disease (GERD), hypothyroidism, asthma, depression and anxiety.

3.5 Tissue preparation

Specimens were collected directly after surgery within 30 minutes. The specimens were transported to the research institution in a Biohazardous Styrofoam container with dry ice until stored in a freezer with subzero temperature of -80ºC for a period of time between 4-6 weeks. The tissues were then taken back to be measured with the tr-FRS system, after they were allowed to fully thaw to room temperature. A subsample of 10 matched pair cases were measured directly after surgical excision prior to the freezing process. These ten matched pairs were then re-measured after the 4-6 week period. No external interference or further processing was performed on the tissue in the freezing and thawing process.

3.6 Measurement Procedure

Figure 8 shows the typical specimen size relative to the petri dish. A small piece of tumour tissue was provided from surgery, with a minimum size requirement of 4×3×2 mm and weighed an average of 20-30 mg. A further small piece of normal tissue with equivalent size was taken at a farther distance from the tumour area to avoid any boundary effects.

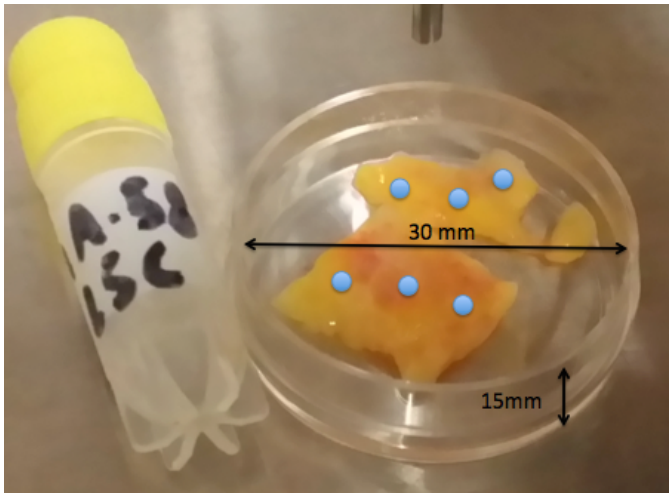

Figure 8: An image of a sample breast tissue in a patri-dish with dimensions 30 mm x 15 mm. Blue dots represent the approximate measurement locations, where each location was measured three times.

Measurements were performed on three locations on each specimen, as marked in the above figure. One central and two peripheral spots were chosen. Measurements were run three times on each location.

3.7 TRF Data Collection

After system initialization, the fluorescence decay, fluorescence steady-state spectra and diffuse reflectance spectra are collected in sequence. Total data acquisition time is about 2 seconds for both TRF and DRS data collection, making the system suitable for

intraoperative purposes. After data collection, the TRF ad DRS data are saved in separate files for subsequent off-line data analysis.

3.8 DRS Data Collection

After TRF data collection, the pulse generator is used to switch between data collection modes. DRS measurements were conducted in the dark to minimize any interference from external photons. DRS system initialization is performed by using the broadband source, with its spectrum shown in figure 9, to illuminate a white piece of paper and adjusting the response signals from the three fibres correlating to the different detector-source distances to be as closely aligned to each other as possible. This ensures the signals coming from each fiber are similar to each other.

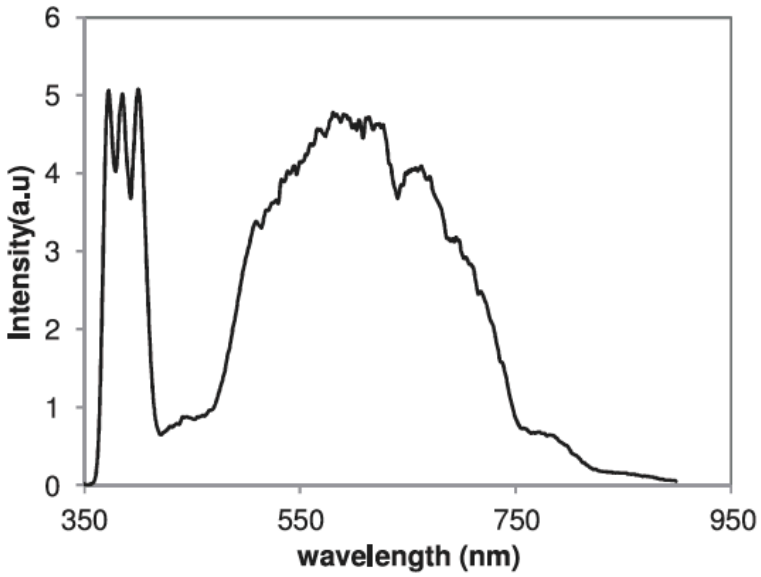

Figure 9: A plot showing the diffuse reflectance spectra of the broadband source.

Optical properties were extracted from the diffuse reflectance by an inverse Monte Carlo approach, displayed as a look up table in reference (Cappon et al., 2013).

Chapter 4: Results Part I; Comparison between fresh and pre-frozen breast samples

4.1 Introduction

The novelty in this work is the measurement of ex-vivo intact breast tissue using the tr-FRS system after immediate surgical excision and re-measurement after freezing for duration of 4-6 weeks and thawing. This was performed to compare between fresh and pre-frozen breast tissue to assess the effects of the freezing and thawing process on the fluorescence and diffuse reflectance response and to validate the use of pre-frozen tissue. Should there be no significant differences between fluorescence lifetime, fluorescence intensity and diffuse reflectance between fresh and pre-frozen breast samples, it can be justified using pre-frozen tissue to build classification models using the tr-FRS data and to predict unknown freshly excised samples.

4.2 Methodology

Tissue measurement specifications and handling are described in section 3.5 and 3.6. In this comparison study, ten matched pair cases were measured with the tr-FRS system twice. The first measurement was conducted directly after surgical excision of the breast tissue and will be referred to as "fresh" in the remaining results and discussion. After data collection, the fresh tissues were frozen from room temperature to a freezer with subzero temperature of -80ºC for a period of time between 4-6 weeks and remeasured after complete thawing of tissue. These tissues will be referred to as "pre-frozen". This temperature was chosen to avoid mechanical changes proven to cause Collagen damage with use of snap freezing using liquid nitrogen (-196ºC) (Szarko et al., 2010). Thawing

was accomplished by exposing tissue to room temperature for a few minutes. No external interference or further processing was done.

4.3 Results

4.3.1 Fluorescence Lifetime

Figure 10 displays the range, median and inter-quartile range (IQR) of the levels for each of the lifetimes at 400nm, 460nm and 515nm corresponding to the emission wavelength of the endogenous fluorophores Collagen, NADH, and FAD respectively within breast tissue. The boxplots display differences in lifetime at each of these wavelengths between tumour and normal breast tissue where lifetime in tumour is significantly higher at 400nm and significantly lower at 460 nm and 515 nm than normal in both fresh (a) and pre-frozen (b) breast tissue.

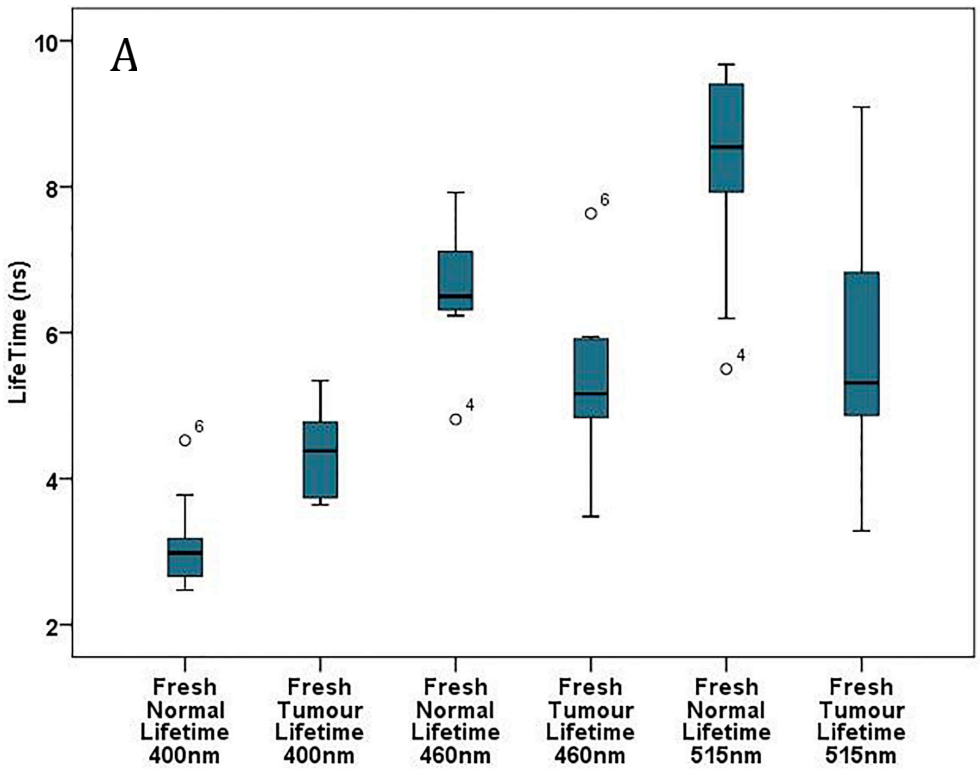

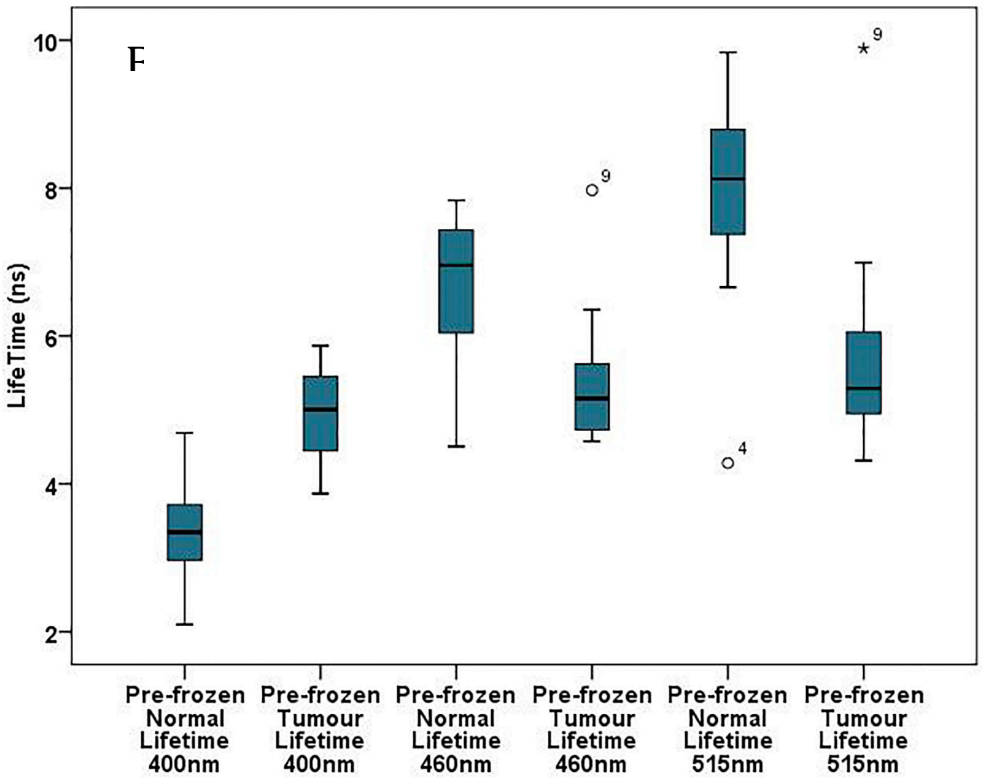

Figure 10: Box plot representation of average lifetime of fresh normal and tumour (A) and defrosted normal and tumour (B) breast tissue at 400 nm, 460 nm, and 515 nm. Significant differences between normal and tumour breast tissue at 400 nm, 460 nm and 515 nm can be seen in both the fresh and pre-frozen sets. ºRepresents outliers with values greater than 1.5 times the IQR *Represents strikes for values greater than 3 times the IQR.

Table 3 looks at the fluorophore lifetime between normal and tumour breast tissue in both fresh and pre-frozen conditions. Significant differences were observed at 400nm, 460nm, and 515nm between normal and tumour in both subsets.

	Fresh			Pre-Frozen		
	Mean (ns)	Standard Error	P-value	Mean (ns)	Standard Error	P-value
Normal Lifetime 400 nm	3.126	.194	P<0.01*[1]	3.391	0.247	P<0.01*[1]
Tumour Lifetime 400 nm	4.381	.179		4.921	0.228	
Normal Lifetime 460 nm	6.604	.266	P=0.01*[1]	6.711	0.311	P=0.02*[1]
Tumour Lifetime 460 nm	5.334	.340		5.495	0.323	
Normal Lifetime 515 nm	8.254	.450	P=0.01*[1]	7.830	0.491	P=0.03*[2]
Tumour Lifetime 515 nm	5.818	.508		5.841	0.510	

Table 3: Lifetime at 400 nm, 460 nm, 515 nm in freshly excised and pre-frozen normal and tumour breast samples (n=10).
Paired-Samples T Test[1]
Wilcoxon Signed Ranks test[2]

*Statistically significant at P<0.05.

Table 4 compares fresh with pre-frozen normal and tumour breast tissue at 400nm, 460nm and 515nm, respectively. No significant difference was observed between the normal fresh and pre-frozen samples and between the tumour fresh and pre-frozen samples. This suggests that the freezing and thawing process did not yield significant changes on the fluorescence lifetime.

	Normal			Tumour		
	Mean (ns)	Standard Error	P-value	Mean (ns)	Standard Error	P-value
Fresh Lifetime 400 nm	3.126	0.194	P=0.30[1]	4.381	0.179	P=0.05[1]
Pre-frozen Lifetime 400 nm	3.391	0.247		4.921	0.228	
Fresh Lifetime 460 nm	6.605	0.266	P=0.66[1]	5.334	0.341	P=0.88[2]
Pre-frozen Lifetime 460 nm	6.711	0.311		5.495	0.323	
Fresh Lifetime 515 nm	8.255	0.451	P=0.25[1]	5.818	0.508	P=0.72[2]
Pre-frozen Lifetime 515 nm	7.830	0.491		5.841	0.510	

Table 4: Lifetime at 400 nm, 460 nm, 515 nm in freshly excised and pre-frozen normal and tumour breast samples (n=10).
Paired-Samples T Test[1]
Wilcoxon Signed Ranks test[2]
Significance tested at P<0.05.

4.3.2 Fluorescence Intensity

Figure 11 shows fluorescence intensity spectra normalized to the applied voltage and is represented as arbitrary units normalized to the maximum NADH peak value of 460nm. The spectra were analyzed using Peak Fit software (PeakFit TM v.4.12, Seasolve Software Inc.) where the emission peaks of fluorophores (collagen at 400 nm, NADH at 460 nm and FAD at 515 nm) were smoothed and treated as Gaussian distributions to determine the amplitude, FWHM and integral area of each fluorophore and can be used as distinguishing parameters in the classification model. For each peak, the integral area was determined by PeakFit using the following FWHM and amplitude equation:

$$y = a\exp\left(-\ln(2)\left(\frac{x - x_0}{dx}\right)^2\right)$$

where a is the amplitude represented in arbitrary units, dx is the half width at half maximum (HWHM) and x_0 is the maximum position.

Figure 11 below shows the emission spectra of fluorophore intensity as a function of wavelength from 370- 550 nm in (A) fresh normal and tumour breast samples and (B) pre-frozen normal and tumour breast samples.

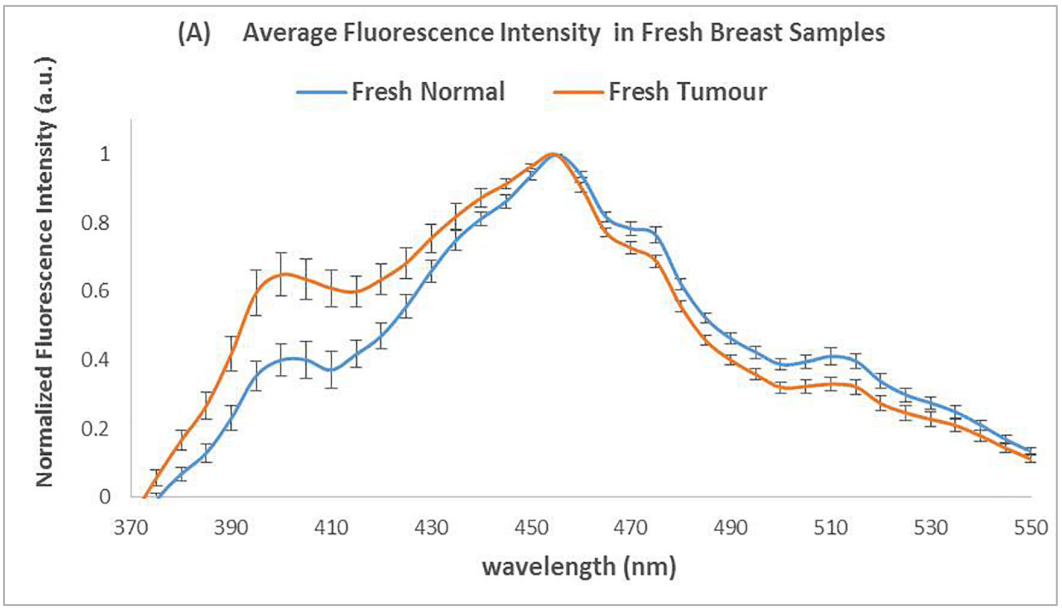

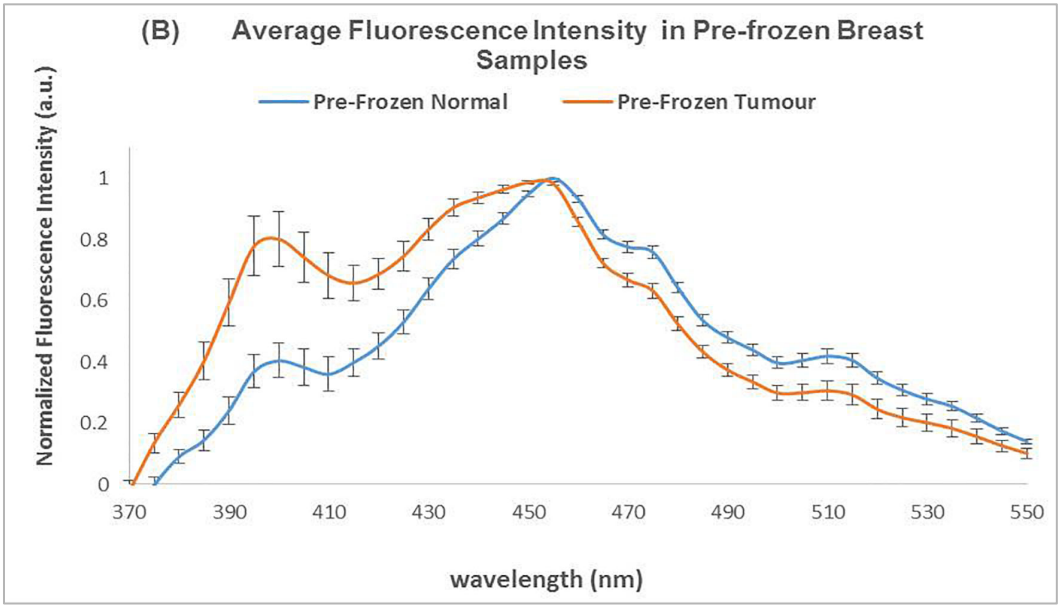

Figure 11: Average fluorescence intensity in fresh normal and fresh tumour breast samples (A) and pre-frozen normal and tumour breast samples (B). Collagen produces an emission spectrum peaking at 390-400 nm, whereas reduced nicotinamide adenine dinucleotide (NADH), and flavin adenine dinucleotide (FAD) emit at 450 nm and 510 nm respectively when induced with a UV laser source of 355 nm. Errors are SE of the mean. Collagen taken at 400 nm, NADH at 460 nm and FAD at 510nm (n=10).

Table 5 represents integral area of collagen, FAD and NADH/FAD in freshly excised and pre-frozen normal and tumour breast tissue (n=10), respectively.

	Fresh			Pre-Frozen		
	Mean (ns)	Standard Error	P-value	Mean (ns)	Standard Error	P-value
Normal Collagen Area	10.227	1.807	P=0.02[*1]	10.199	1.702	P<0.01[*1]
Tumour Collagen Area	20.035	2.861		23.529	3.039	
Normal FAD Area	16.776	.882	P=0.29[1]	17.655	1.379	P=0.02[*2]
Tumour FAD Area	15.207	1.355		13.671	1.829	
Normal NADH to FAD Area	3.483	.186	P=0.29[1]	3.432	0.372	P<0.01[*1]
Tumour NADH to FAD Area	3.906	.401		4.687	0.497	

Table 5: Collagen integral area, FAD integral area, and NADH/FAD integral area in freshly excised and pre-frozen normal and tumour breast tissue (n=10).
Paired-Samples T Test[1]
Wilcoxon Signed Ranks test[2]
*Statistically significant at P<0.05.

A direct comparison between freshly excised and pre-frozen normal breast tissue is demonstrated in figure 12A followed by freshly excised and pre-frozen tumour breast tissue in figure 12B.

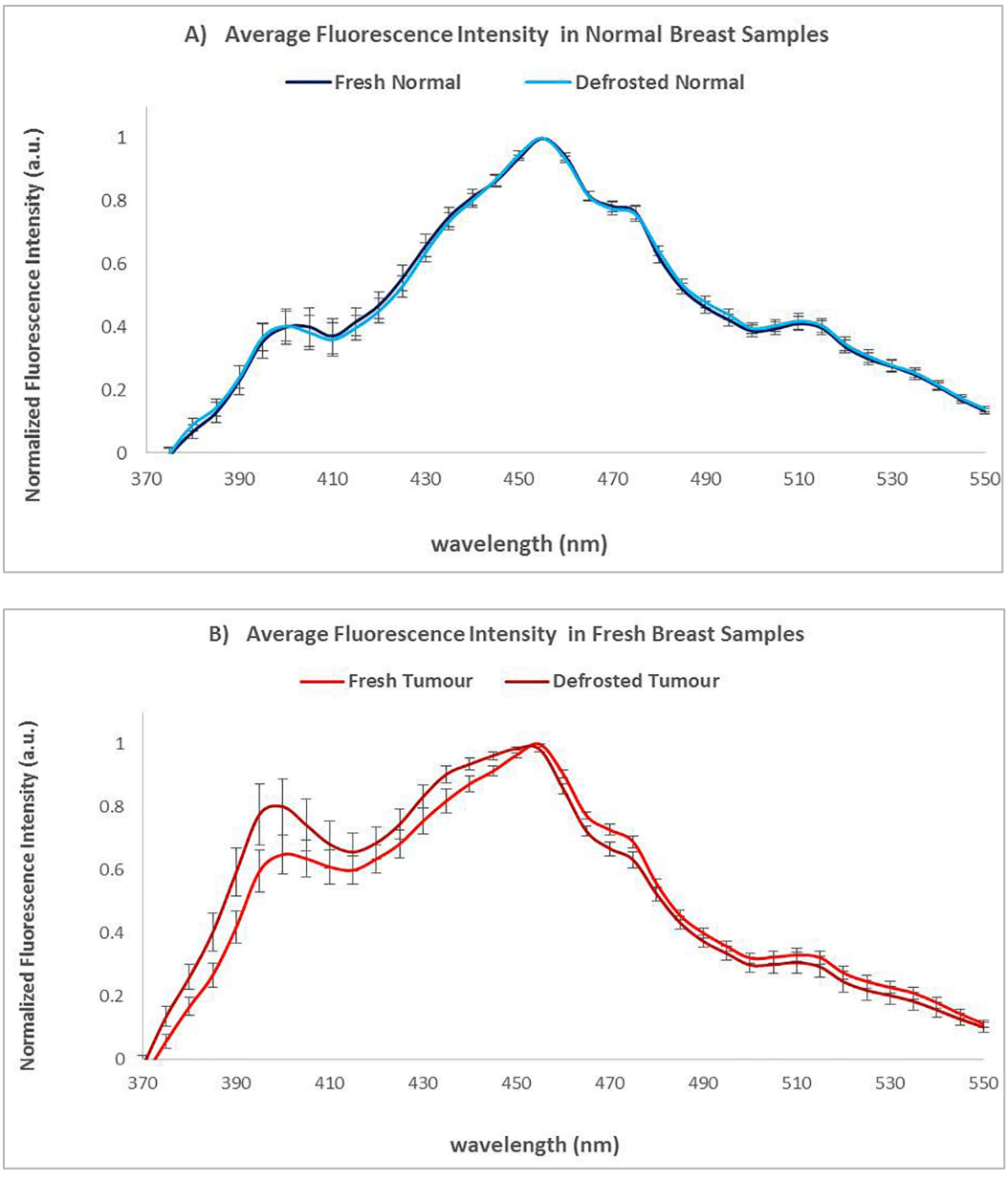

Figure 12: Direct comparison of average fluorescence intensity in fresh normal and pre-frozen normal breast samples (A) and fresh and pre-frozen tumour breast samples (B). Errors are SE of the mean. Collagen taken at 400 nm, NADH at 455nm-460 nm and FAD at 510nm (n=10).

Table 6 shows collagen integral area in freshly excised and pre-frozen between normal and tumour breast tissue (n=10).

	Mean	Std. Error	P value
Fresh Normal Collagen Area	10.227	1.807	P=0.99[1]
Pre-frozen Normal Collagen Area	10.199	1.702	
Fresh Tumour Collagen Area	20.035	2.862	P=0.28[1]
Pre-frozen Tumour Collagen Area	23.528	3.038	

Table 6: Collagen integral area in freshly excised and pre-frozen normal and tumour breast tissue (n=10).
Paired-Samples T Test[1]
Significance tested at P<0.05.

Table 7 shows FAD integral area in freshly excised and pre-frozen between normal and tumour breast tissue (n=10).

	Mean	Std. Error	P value
Fresh Normal FAD Area	16.777	0.882	P=0.46[1]
Pre-frozen Normal FAD Area	17.655	1.379	
Fresh Tumour FAD Area	15.208	1.356	P=0.39[2]
Pre-frozen Tumour FAD Area	13.671	1.829	

Table 7: FAD integral area in freshly excised and pre-frozen normal and tumour breast tissue (n=10).
Paired-Samples T Test[1]
Wilcoxon Signed Ranks test[2]
Significance tested at P<0.05.

Table 8 shows NADH/FAD integral area in freshly excised and pre-frozen between normal and tumour breast tissue (n=10).

	Mean	Std. Error	P value
Fresh Normal NADH to FADH Area	3.483	0.187	P=0.88[1]
Pre-frozen Normal NADH to FADH Area	3.432	0.372	
Fresh Tumour NADH to FAD Area	3.906	0.401	P=0.21[1]
Pre-frozen Tumour NADH to FAD Area	4.687	0.497	

Table 8: NADH/FAD integral area in freshly excised and pre-frozen normal and tumour breast tissue (n=10).
Paired-Samples T Test[1]
Significance tested at P<0.05.

Table 6, 7, and 8 show no significant difference between fresh normal breast tissue and pre-frozen normal breast tissue in collagen, FAD and NADH/FAD integral area. There was also no significant difference between freshly excised tumour breast tissue and pre-frozen tumour breast tissue in collagen, FAD and NADH/FAD integral area.

4.3 Diffuse Reflectance

4.3.1 Absorption Coefficient

The absorption coefficient is directly related to tissue absorber concentration and saturation such as oxygenated and de-oxygenated hemoglobin and beta carotene. The scattering coefficient relies on information on the size and density of scattering centers in tissue, such as cells and nuclei which have been shown to be significantly different between malignant and normal tissue (Zhu et al., 2006a). The optical properties (absorption coefficient and reduced scatter coefficient) of the tissue can be extracted from the diffuse reflectance spectra using a lookup table. This method is explained in detail by Rajaram (Rajaram et al., 2008).

Table 9 compares the absorption coefficient between fresh and pre-frozen normal and tumour breast tissue at 545nm and 575 nm. No significant difference was observed for both the normal and tumour subset.

	Normal			Tumour		
	Mean (mm^{-1})	Standard Error	P-Value	Mean (mm^{-1})	Standard Error	P-Value
Fresh Absorption coefficient 545 nm	5.735	1.281	P=0.43[1]	5.208	0.624	P=0.13[1]
Pre-frozen Absorption coefficient 545 nm	6.598	1.188		7.141	1.528	
Fresh Absorption coefficient 575 nm	6.033	1.389	P=0.59[1]	5.229	0.623	P=0.14[2]
Pre-frozen Absorption coefficient 575 nm	6.702	1.265		7.507	1.651	

Table 9: Absorption coefficient at 545 nm and 575 nm for fresh and pre-frozen normal and tumour breast tissue (n=10).
Paired-Samples T Test[1]
Wilcoxon Signed Ranks test[2]
Significance tested at P<0.05.

4.3.2 Reduced Scatter Coefficient

Table 10 compares the reduced scatter coefficient between normal and tumour fresh and pre-frozen breast tissue at 545nm and 575 nm.

	Normal			Tumour		
	Mean (mm^{-1})	Standard Error	P-Value	Mean (mm^{-1})	Standard Error	P-Value
Fresh reduced scatter coefficient 545 nm	15.814	1.745	P=0.21[1]	17.310	1.415	P=0.05[2]
Pre-frozen reduced scatter coefficient 545 nm	17.756	1.869		21.952	1.607	
Fresh reduced scatter coefficient 575 nm	15.180	1.675	P=0.21[1]	16.616	1.358	P=0.05[2]
Pre-frozen reduced scatter coefficient 575 nm	17.044	1.794		21.072	1.542	

Table 10: Reduced scatter coefficient at 545 nm and 575 nm for fresh and pre-frozen normal and tumour breast tissue (n=10).
Paired-Samples T Test[1]
Wilcoxon Signed Ranks test[2]
Significance tested at P<0.05.

No significant differences in absorption coefficient and reduced scatter coefficient were observed for both the normal and tumour subset in tables 9 and 10. This implies that the freezing and thawing process did not contribute to significant differences in optical properties.

4.4 Discussion

This work shows the capability of the tr-FRS system to differentiate between normal and tumour breast tissue. Collagen area, lifetime at 400nm, 460nm and 515nm are significantly different between tumour and normal in both fresh and pre-frozen breast tissue. FAD integral area was significantly higher in pre-frozen tumour than pre-frozen normal breast samples whereas no significant differences were observed between the fresh tumour and fresh normal breast samples. NADH/FAD integral area was also significantly higher in pre-frozen tumour than pre-frozen normal breast samples. However no significant differences were observed in NADH/FAD integral area between the fresh tumour and fresh normal breast samples. These results showed that the process of freezing and thawing did not cause any significant differences between normal fresh and normal pre-frozen breast tissue or between tumour fresh and tumour pre-frozen breast tissue. There were no significant differences in fluorescence lifetime at 400 nm, 460 nm and 515 nm as well as collagen area, FAD area, NADH/FAD area, absorption coefficient at 545 nm and 575 nm as well as the reduced scatter coefficient at 545 nm and 575 nm between fresh and pre-frozen samples. This justifies the suitability of using archived frozen tissue bank specimens to increase the data set used for designing the mathematical models required to differentiate tumour and normal samples.

A study by Palmer, et al. reported that freezing and thawing of tissues lead to a decrease in the diffuse reflectance signal compared with the freshly excised breast tissue. This lower diffuse reflectance signal suggests an increase in tissue absorption most likely due to an increase in the effect of hemoglobin absorption. This might also be the effect of cell lysing brought by the freezing and thawing process. However, our study showed no

significant differences between normal and tumour absorption coefficient in both the fresh and pre-frozen samples. Therefore no significant difference between the fresh and pre-frozen normal as well as the fresh and pre-frozen tumour does not reveal any useful information on whether the absorption coefficient is altered by the freezing and thawing process.

4.5 Conclusion

Based on our pilot clinic results, limited by the small sample size (n=10), we aim to obtain more cases to increase our data set to validate the above results. The results of this study show the validity of using archived frozen breast tissues from a tissue bank to simulate the fluorescence response and optical properties of fresh breast tissue. This allows for the development of classification models using pre-frozen breast tissue that could be used in-vivo real time at the time of surgery to differentiate tumour from normal tissue.

Chapter 5: Results Part II; Comparison between normal and tumour breast samples

5.1 Histology

After data has been collected, the tissue sample is fixed in 10% buffered formalin for at least 24 hours and returned to the hospital for histological analysis and processed using a vacuum infiltration tissue processor (VIP) overnight. The tissue is then embedded in paraffin and cut into 4 microns thick slices with a microtome. The sections are stained with Hematoxylin and Eosin (H&E) and analyzed under the microscope. A first scan is made with a low power for an overview and then analyzed under high power. The uneven distribution of the tumor allows for a 400 magnification scan of the area to be made in order to be able to measure the amount of tumour with a micrometer and calculate a percentage of tumour. The amount of tumour cells, surrounding connective tissue and fat was evaluated using this semi-quantitative technique.

Figure 13 below display the histological images of a (A) normal breast sample mostly consisting of adipose tissue, a normal more dense tissue (B) with higher fibrous content and a tumourous breast (C) displaying increased cell density marked by darker nuclei in comparison to the normal tissue.

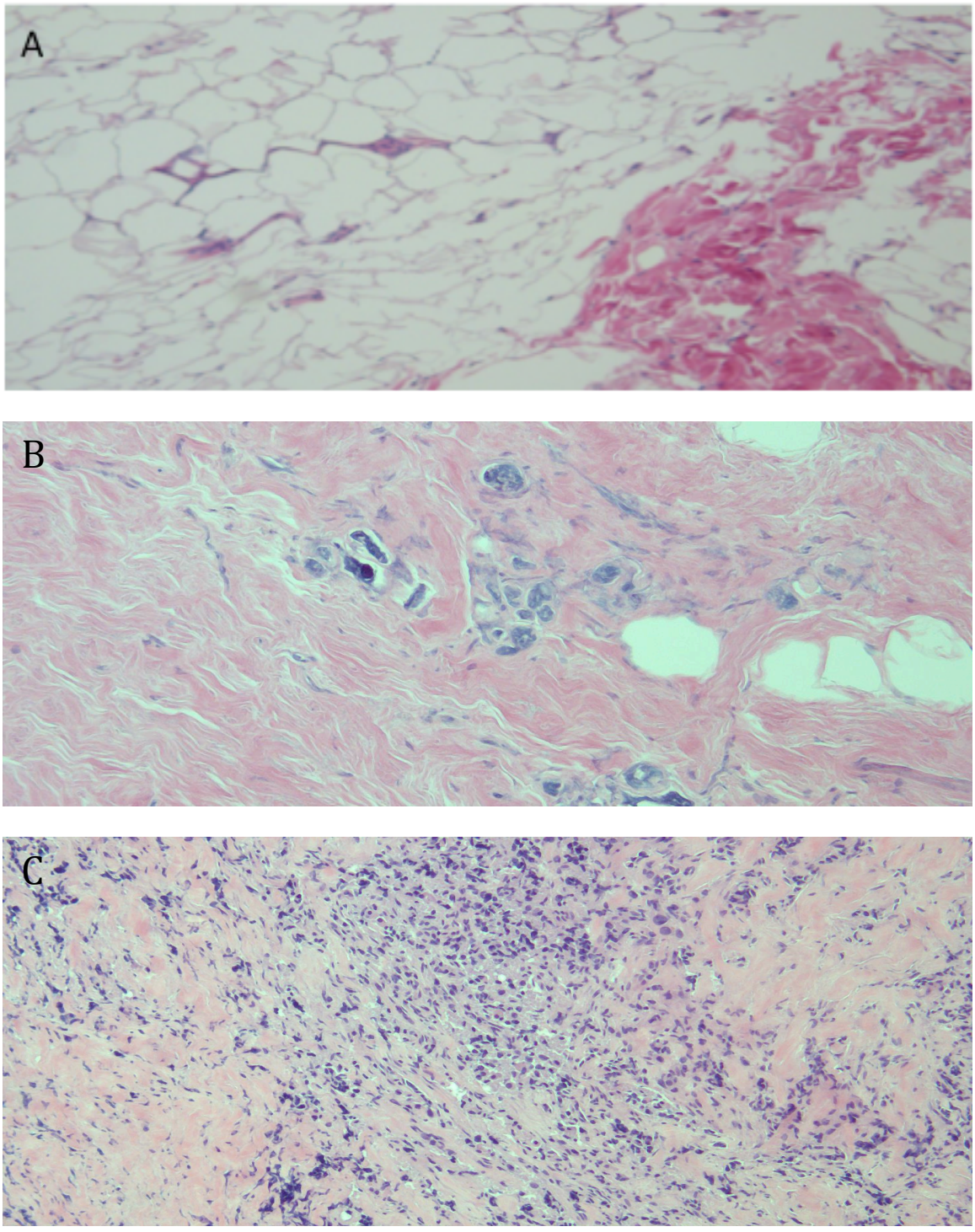

Figure 13: Breast samples stained with H&E showing A) normal breast with high adipose tissue, B) normal breast with high fibrous tissue content and C) tumour breast samples showing increased nuclei and cell density.

Table 11 below lists the histological results for all samples collected for this study from patients undergoing BCS.

CASE NUMBER	Normal/Fat Content (%)	Tumour Content (%)	CASE NUMBER	Normal/Fat Content (%)	Tumour Content (%)
IMA 3	90	70	IMA 38	90	80
IMA 4	Cancer	10	**IMA 39**	20	50
IMA 6	30	80	**IMA 41**	95	No Cancer
IMA 7	50	90	IMA 42	20	90
IMA 13	90	50	IMA 44	90	85
IMA 14	20	80	IMA 45	95	50
IMA 15	40	50	IMA 46	50	80
IMA 16	20	40	**IMA 47**	95	90
IMA 18	60	60	IMA 49	50	50
IMA 19	30	10	IMA 50	60	60
IMA 20	40	15	IMA 52	80	90
IMA 21	80	60	IMA 54	80	80
IMA 22	80	75	**IMA 55**	Cancer (60%)	10
IMA 24	90	90	IMA 56	40	80
IMA 25	10	90	IMA 57	80	40
IMA 26	60	90	IMA 58	80	80
IMA 28	80	60	**IMA 59**	50	60
IMA 30	90	90	IMA 60	20	80
IMA 31	99	95	IMA 61	20	100
IMA 32	90	60	IMA 62	95	60
IMA 33	80	90	**IMA 63**	90	90
IMA 34	80	80	**IMA 65**	Cancer (90%)	70
IMA 35	20	90	IMA 66	90	90
IMA 36	60	80	IMA 67	50	50

Table 11: Histological analysis on 48 matched pair cases showing the fat content in the normal samples and the tumour content in the tumour samples.

Although 50 matched pair cases were collected and measured, histological analysis was conducted on 48 samples and revealed inconclusive results on an additional 8 matched pair cases where 3 normal samples (IMA 4, 55, 65) contained tumour, one tumour sample (IMA 41) was in fact normal and contained 0% tumour and 4 cases (IMA 14, 49, 60, 63) contained high density of necrotic cells. These 8 matched pair cases were omitted and all statistical and mathematical modeling results were based on the 40 matched pair cases.

5.2 Statistical Analysis

All statistical analysis was performed using IBM SPSS Statistics Version 22. The *P* value has been reported for each variable as $P<0.05$ being significant. The Shapiro-test was used for each category to test if the data set was consistent with a Gaussian distribution function. Wilcoxon Signed Ranks Test was used for comparing the difference of the parameters for non-normally distributed data while a Paired-Sample T Test was used with a 95% confidence level in order to investigate the significant parameters for normally distributed data.

5.2.1 Fluorescence Lifetime

In figure 14 below boxplots are displayed showing, the range, median and inter-quartile range (IQR) of the levels for each of the lifetimes at 400nm, 460nm and 515nm corresponding to the emission wavelength of the endogenous fluorophores collagen, NADH, and FAD respectively within breast tissue. The boxplots display differences in lifetime at each of these wavelengths between tumour and normal breast tissue. Fluorescence lifetime in tumour is significantly higher at 400nm ($p<0.01$) and significantly lower ($p<0.01$) at 460 nm and 515 nm than normal.

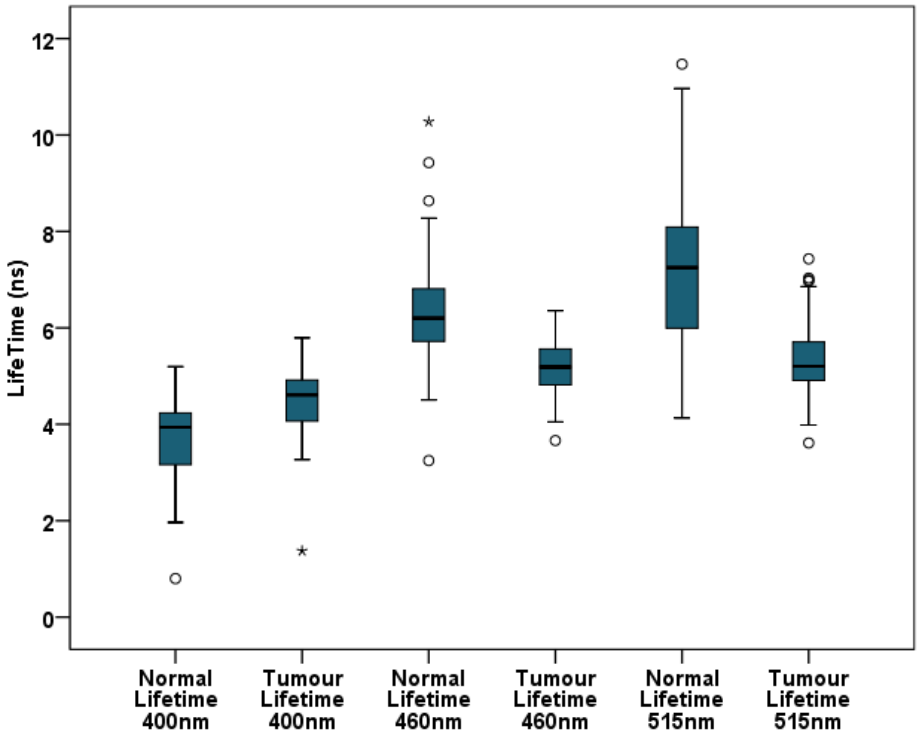

Figure 14: Box plot representation of average lifetime of normal and tumour breast tissue at 400 nm, 460 nm, and 515 nm. ºRepresents outliers with values greater than 1.5 times the IQR *Represents strikes for values greater than 3 times the IQR.

Table 12 shows the lifetime values at 400, 460 and 515 nm, the wavelength corresponding to collagen, NADH and FAD emissions respectively.

	Mean (ns)	Std. Error	P-value
Normal Lifetime 400 nm	3.567	0.138	P<0.01*[2]
Tumour Lifetime 400 nm	4.318	0.205	
Normal Lifetime 460 nm	6.342	0.172	P<0.01*[1]
Tumour Lifetime 460 nm	5.141	0.097	
Normal Lifetime 515 nm	7.411	0.238	P<0.01*[1]
Tumour Lifetime 515 nm	5.261	0.138	

Table 12: Lifetime at 400 nm, 460 nm, 515 nm in pre-frozen normal and tumour breast samples (n=40).
Paired-Samples T Test[1]
Wilcoxon Signed Ranks test[2]
*Statistically significant at P<0.05.

5.2.2 Fluorescence Intensity

Please refer to section 4.3.2 for the normalization and fitting of the fluorescence intensity.

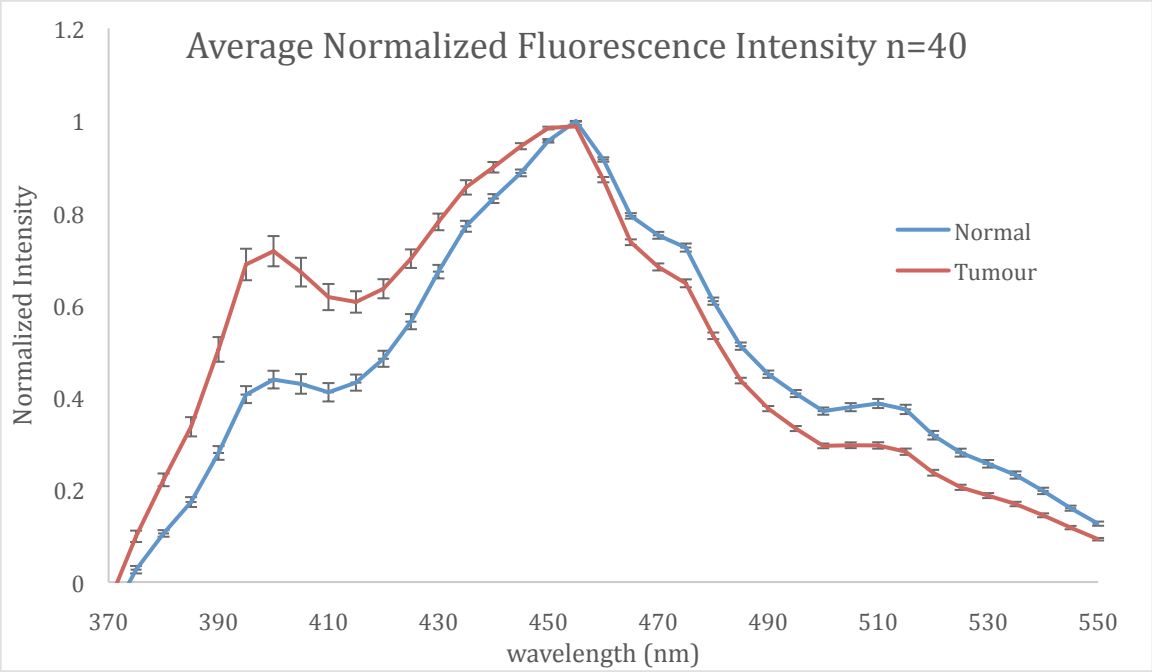

Figure 15: Average fluorescence intensity in normal tumour breast samples (n=40). Collagen produces an emission spectrum peaking at 390-400 nm, whereas reduced nicotinamide adenine dinucleotide (NADH), and flavin adenine dinucleotide (FAD) emit at 460 nm and 510 nm respectively when induced with a UV laser source of 355 nm. Errors are SE of the mean. Emission peaks of collagen, NADH and FAD were taken at 400, 460 and at 510 nm, respectively.

Table 13 shows the collagen amplitude and integral area between normal and tumour breast samples.

	Mean (a.u.)	Std. Error	P-value
Normal Collagen Amplitude	0.368	0.022	P<0.01*[1]
Tumour Collagen Amplitude	0.572	0.030	
Normal Collagen Area	9.746	0.661	P<0.01*[1]
Tumour Collagen Area	15.778	0.899	

Table 13: Collagen amplitude, FWHM, and integral area of Collagen in normal and normal breast tissue taken at 400 nm (n=40).
Wilcoxon Signed Ranks test1
*Statistically significant at P<0.05.

Table 14 shows the NADH amplitude and integral area between normal and tumour breast samples taken at 460 nm.

	Mean (a.u.)	Std. Error	P-value
Normal NADH Amplitude	0.971	0.002	P<0.01*[1]
Tumour NADH Amplitude	0.986	0.029	
Normal NADH Area	60.720	0.718	P=0.03*[1]
Tumour NADH Area	62.517	0.849	

Table 14: NADH amplitude, FWHM, and integral area of NADH in normal and normal breast tissue taken at 460 nm (n=40).
Paired-Samples T Test[1]
*Statistically significant at P<0.05.

Table 15 shows the FAD amplitude and integral area between normal and tumour breast samples taken at 510 nm.

	Mean (a.u.)	Std. Error	P-value
Normal FAD Amplitude	0.332	0.011	P<0.01*[1]
Tumour FAD Amplitude	0.258	0.008	
Normal FAD Area	13.659	0.609	P<0.01*[1]
Tumour FAD Area	9.935	0.429	

Table 15: FAD amplitude, FWHM, and integral area of FAD in normal and normal breast tissue taken at 510 nm (n=40).
Paired-Samples T Test[1]
*Statistically significant at P<0.05.

Table 16 shows the NADH/FAD amplitude and integral area between normal and tumour breast samples.

	Mean (a.u.)	Std. Error	P-value
Normal NADH to FAD Amplitude	3.07	0.118	P<0.01*[1]
Tumour NADH to FAD Amplitude	3.978	0.131	
Normal NADH to FAD Area	4.88	0.276	P<0.01*[1]
Tumour NADH to FAD Area	6.854	0.362	

Table 16: NADH to FAD amplitude, FWHM, and integral area in normal and normal breast tissue (n=40).
Wilcoxon Signed Ranks test[1]
*Statistically significant at P<0.05.

Figure 16 displays the average diffuse reflectance spectra from fibre 1 between normal and tumour breast samples from the 420-670 nm range.

5.2.3 Diffuse Reflectance

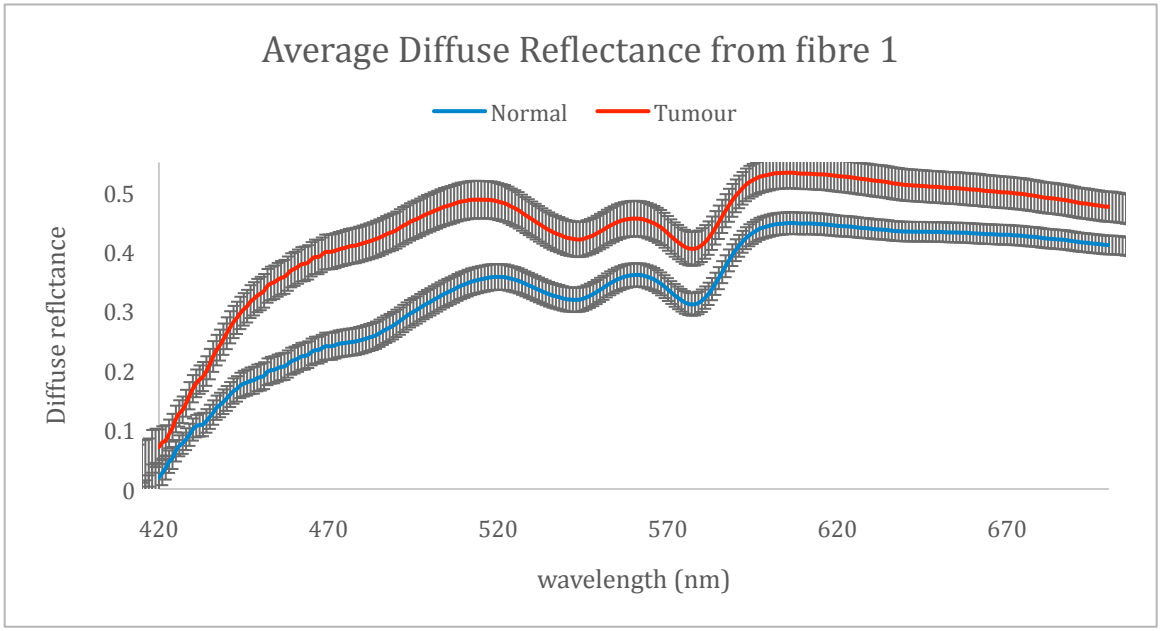

Figure 16: Diffuse reflectance (DR) spectra of tumour and normal breast tissue from fibre 1 (n=40). Tumour samples showing significantly higher DR than normal samples. Errors are SE of the mean.

In table 17 below, the average diffuse reflectance from fibre 1 at 545 and 575 nm, the wavelengths corresponding to the absorption of hemoglobin, is shown.

	Mean (a.u.)	Std. Error	P-value
Normal diffuse reflectance 545 nm	0.312	0.018	P<0.01*[2]
Tumour diffuse reflectance 545 nm	0.409	0.024	
Normal diffuse reflectance 575 nm	0.306	0.018	P<0.01*[1]
Tumour diffuse reflectance 575 nm	0.395	0.023	

Table 17: Diffuse reflectance in normal and tumour breast samples at 545 nm and 575 nm (n=40).
Paired-Samples T Test[1]
Wilcoxon Signed Ranks test[2]
*Statistically significant at P<0.05.

5.2.4 Optical Properties

5.2.4.1 Absorption Coefficient

Figure 17 below displays the average absorption coefficient from 480 to 620 nm between normal and tumour breast samples.

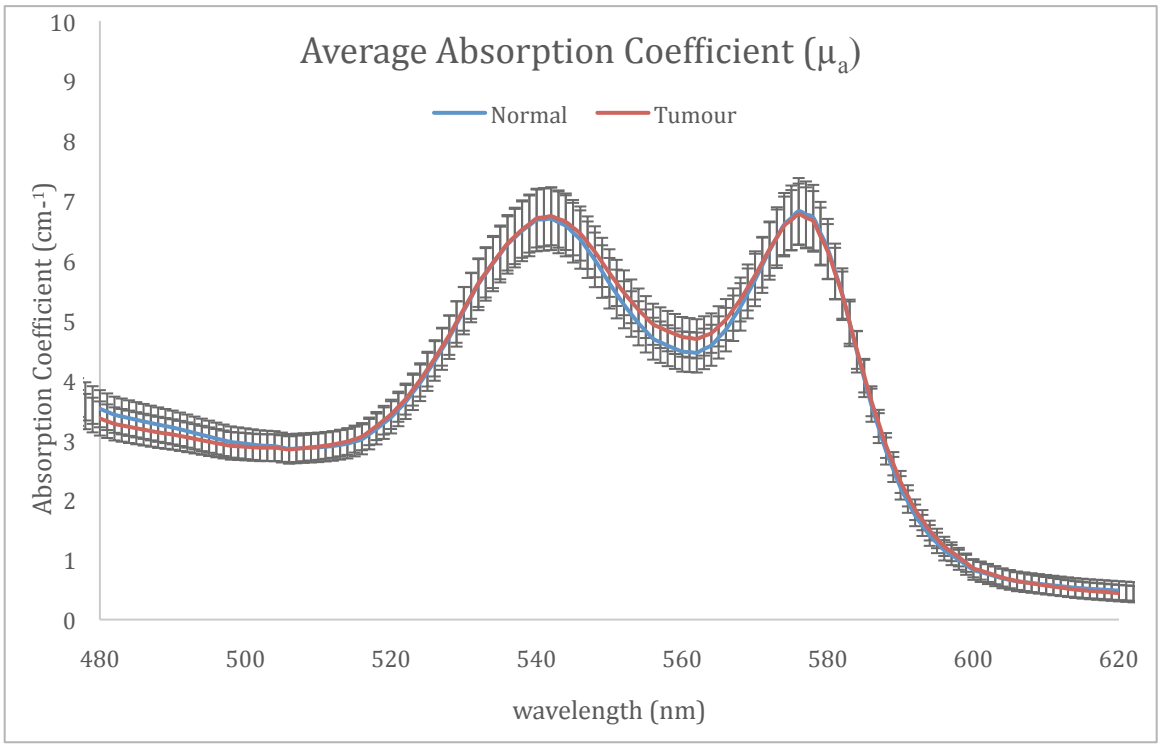

Figure 17: The average absorption coefficient in normal and tumour breast samples (n=40). Errors are SE of the mean.

Table 18 represents the average absorption coefficient in normal and tumour breast samples at 545 and 575 nm.

	Mean (cm^{-1})	Std. Error	P-value
Normal absorption coefficient 545 nm	6.282	0.500	P=0.78[1]
Tumour absorption coefficient 545 nm	6.431	0.436	
Normal absorption coefficient 575 nm	6.484	0.531	P=0.81[2]
Tumour absorption coefficient 575 nm	6.654	0.472	

Table 18: Average absorption coefficient at 545 and 575 nm of normal and tumour breast tissue (n=40).
Paired-Samples T Test[1]
Wilcoxon Signed Ranks test[2]
*Statistically significant at P<0.05.

5.2.4.2 Reduced Scatter Coefficient

Figure 18 displays the average reduced scatter coefficient from 480 to 620 nm between normal and tumour breast samples.

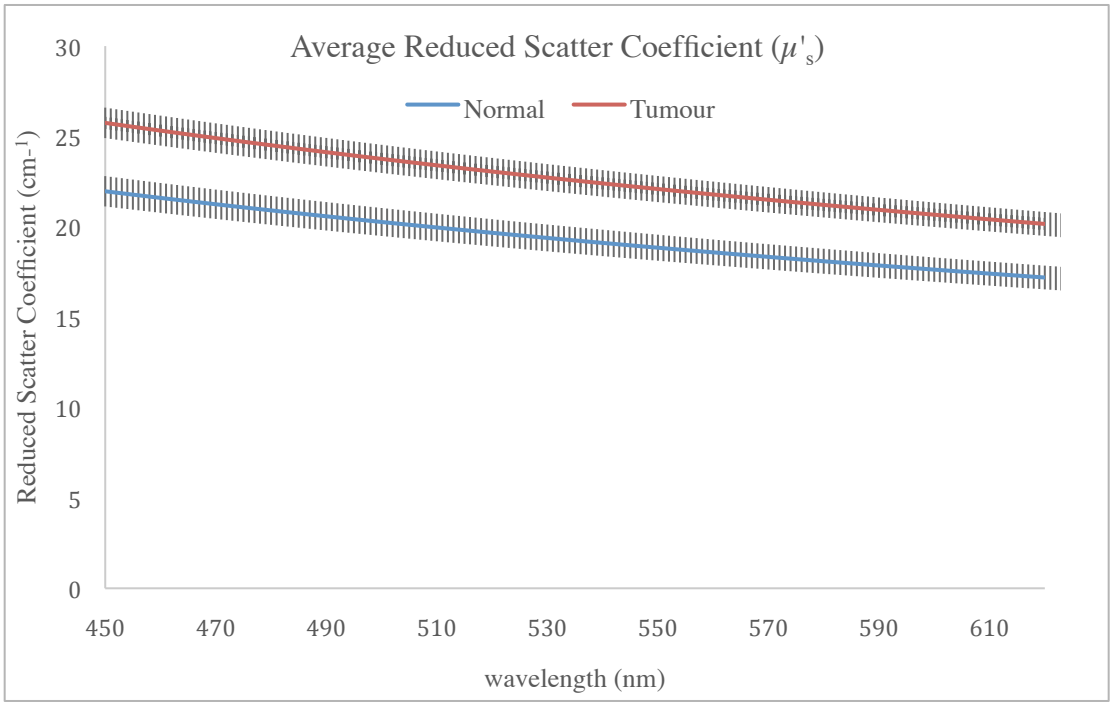

Figure 18: The average reduced scatter coefficient in tumour and normal breast samples (n=40). Errors are SE of the mean.

Table 19 presents the reduced scatter coefficient in normal and tumour breast samples at 545 and 575 nm.

	Mean (cm^{-1})	Std. Error	P-value
Normal reduced scatter coefficient 545 nm	18.571	0.790	P<0.01*[1]
Tumour reduced scatter coefficient 545 nm	22.162	0.721	
Normal reduced scatter coefficient 575 nm	17.826	0.789	P<0.01*[1]
Tumour reduced scatter coefficient 575 nm	21.273	0.692	

Table 19: Average reduced scatter coefficient at 545 and 575 nm of normal and tumour breast tissue (n=40).
Paired-Samples T Test[1]
*Statistically significant at P<0.05.

5.3 Classifications and Prediction

Multivariate data analysis is used for data description (Explorative data structure modeling), discrimination and classification, as well as for regression and prediction. The purpose of all multivariate data analysis is to decompose the data in order to determine and model any hidden phenomena or trends within the data. The revealing of any underlying covariance structure is the backbone of Principle Component Analysis (PCA). PCA is a method used for data description and explorative data structure modeling of any generic dimensional data matrix. PCA can also assign, or classify new objects (in this case; breast tissue) into their respective classes (normal vs tumour) based on measured variables.

The first principle component (PC1) is the central axis that lies along the direction of maximum variance in the data set while Principle Component 2 (PC2) will lie along a direction orthogonal to PC1 and in the direction of the second largest variance, as shown in figure 19 below. PC3 will lie orthogonal to PC1 and PC2 and in the direction of the third largest variance, and so on for PC4 and PC5 etc. All PCs are orthogonal to each other with a common axis and represent successively smaller and smaller spreads of the object (breast samples) data. Thus, the last PC will lie along the directions where there is very little spread in the object and there are no longer any underlying phenomena to stretch out the spread of the data, perhaps representing "noise". It is important to optimize the number of PCs used by keeping the low-order PCs with the highest contributions while removing the noisy high-order PCs.

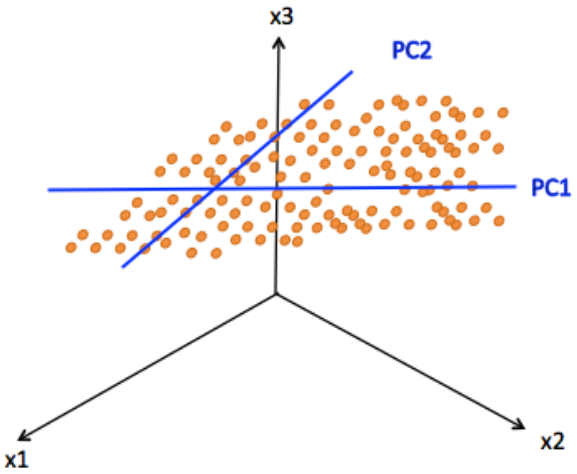

Figure 19: An illustration of the data points (orange) in variable space where x1, x2 and x3 represent different variables. PC1 shows the direction of the maximum variance or spread in the data set. PC2 shows the direction of the second largest variance in the data set.

Since determining the number of optimal PCs is essential in creating an non-noisy but accurate model, the scree plot below in figure 20 can be used to determine how much of the data is accounted for by a certain number of PCs. Scree plots can assist in determining the optimal number of principle components for modeling. Four PC's were used in the construction of the models as well as for tissue classification as that was determined to estimate about 90% of the data while reducing noise within the models.

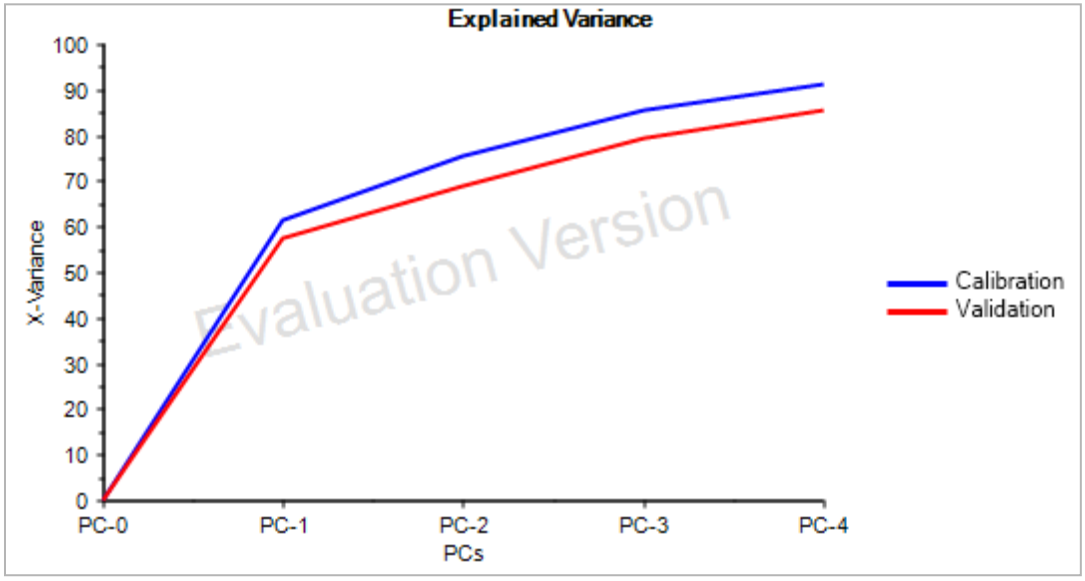

Figure 20: A scree plot showing the calibration and validation of the PCs and the X-variance of the data. Four PCs accounts for about 90% of the data and were used for PC model construction and classification of unknown samples.

PC1 and PC2 can then be plotted on a separate graph as the x and y-axis to show clustering between sets in the data in a comprehendible figure. Figure 21 shows PC1 and PC2 of 40 samples where the normal clusters more to the left and tumour to the right.

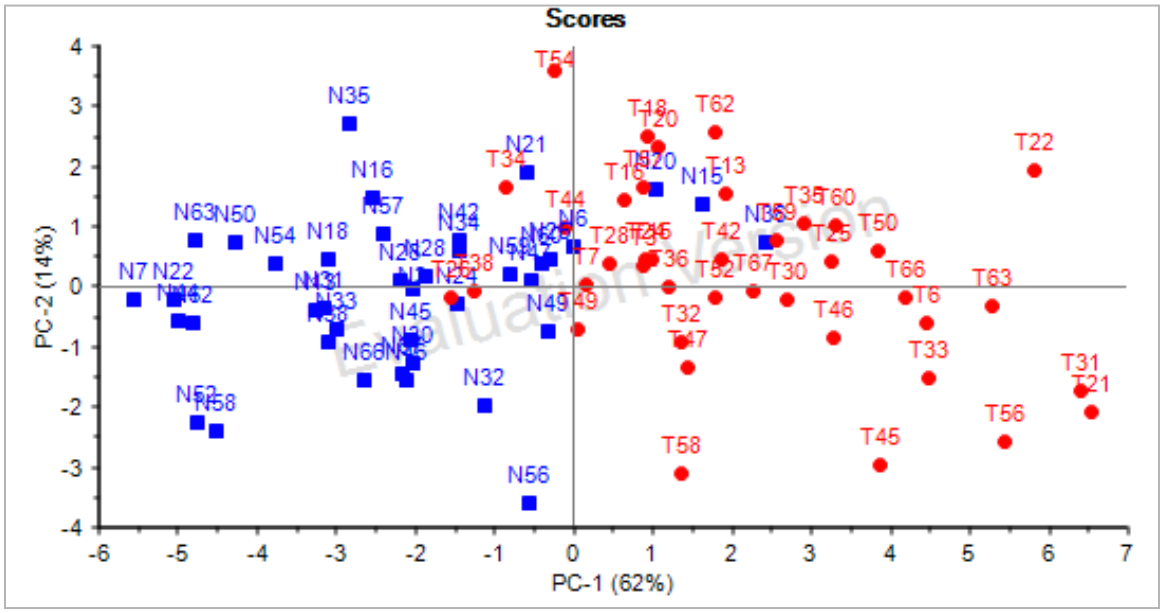

Figure 21: An initial plot of all 40 samples classified as either normal (red) or tumour (blue) plotted in PC space based on histological analysis. Numbers represent case numbers.

Although there is clear clustering of normal samples to the left and tumour samples to the right, and the majority of the data (76%) can be represented by PC1 and PC2, central region around the origin of PC1 and PC2 which displays a sizeable overlap between some tumour and normal breast samples.

Variables that were found to be statistically significant using previous tests were used in the construction of the PC normal and tumour models used in classification. Variables further away from the PC1 axis or PC2 axis are considered strong variables in differentiating between tumour and normal breast samples, whereas variables closer to the origin provide a weaker PCA model. Variables that were insignificant in the statistical analysis were excluded from the construction of the normal and tumour models, as they were also located centrally in the PC plots. Since PCA is a method based on finding directions of maximum variation, it depends on the relative variance of the variables. Weighting of the variables is performed to assign a lighter or heavier importance to each variable along the same scale in a group. The variables used in the model construction were weighed by a factor of 1/SDev. 1/SDev is called standardization and is used to give all variables the same variance. This gives all variables the same chance to influence the estimation of the components. Standardization is often used if the variables are measured with different units; have different ranges; or are of different types.

In figure 22, the statistically significant variables that were used to construct the normal and tumour PCA and their location relative to PC1 and PC2, are shown.

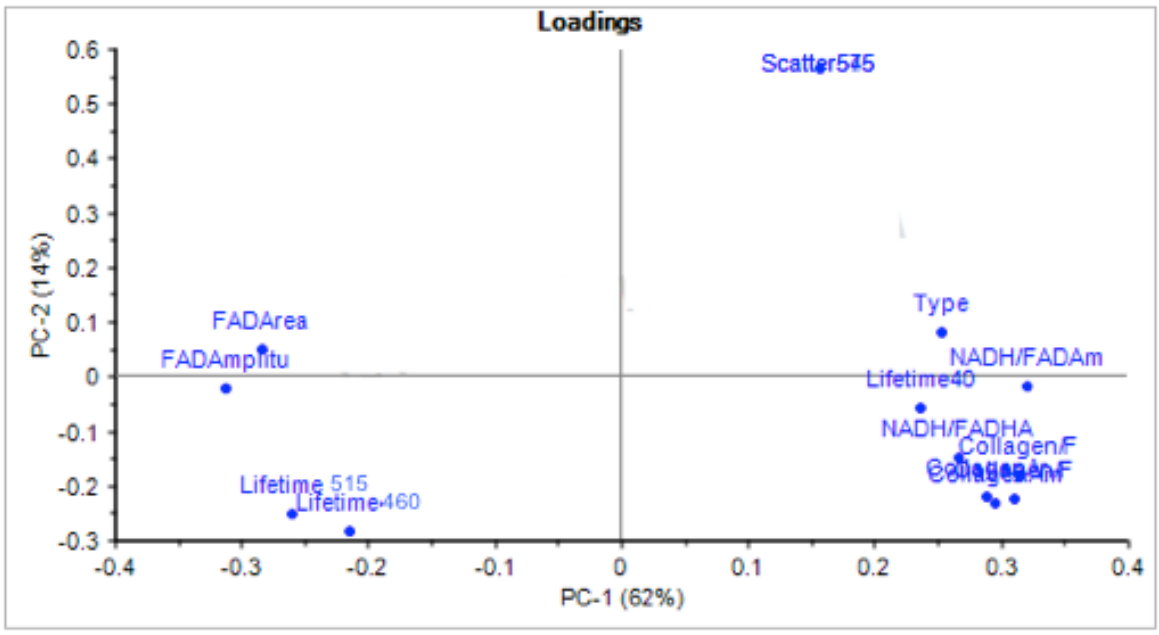

Figure 22: Plot of the statistically significant variables in PC space used to build normal and tumour PCA models. PC1 represents 62% of the data and PC2 represents 14% of the data. A total of 4 PCs were used.

Full chart information including age, smoking status, menopausal status, tumour type and grade, surgery type, estrogen receptor status, progesterone receptor status, were also included in the PC models to investigate whether they provided any beneficial addition to the classification, and were found to be centrally located in the above plot, hence removed.

After construction of the PCA models for both normal and tumour, tissue classification was conducted using Soft Independent Modeling of Class Analogy (SIMCA). SIMCA is a tool that has the potential to classify based on similarity and pattern recognition. It can be used to identify or quantitatively characterize subgroups within a set of samples, and to assess whether a new sample is similar to other samples, or to which group it belongs.

Essentially SIMCA is a classification tool composed of several PC models, one for each individual class identified (i.e normal and tumour). A residual is calculated as the sum of the distance between the sample variable value and the predicted value for each PC. Comparing this test sample variable error with the class membership limit (confidence level) determines whether a test sample may belong to a particular class or not. Each unknown test sample is tested against the individual PCA model. The ability of the system to predict unknown sample membership accurately is dependent on how far apart each of the PCA models appears in PC space. The further apart the component models are, the greater the ability to distinguish between samples. Ideally no membership limits should overlap, as this results in samples belonging to more than one class. The result of SIMCA classification in this study for a test sample could be: 1) normal tissue is correctly predicted as normal, meaning that it fits one model only within the given limits, and also the distance to the next closest group is much larger than the accepted distance of this group, 2) normal tissue is incorrectly predicted as tumour, 3) tumour tissue is correctly predicted as tumour, 4) tumour tissue is incorrectly predicted as normal, 5) The sample may fit both normal and tumour group, meaning that it has a distance that is within the critical limits of both groups simultaneously, recorded as "both" or 6) The sample fits neither normal or tumour group and the result would be recorded as "none".

Table 20 below shows the SIMCA classification results with 5% confidence level from 40 matched pair samples. The jack-knifing technique was used in the prediction of tissue classification; where one sample was randomly removed and a normal and tumour PCA model were build using every sample except the randomly removed sample. The models were then used to classify the randomly removed sample as either belonging to the

normal PCA model, tumour PCA model, both normal and tumour PCA or neither. This technique was conducted on each sample.

	Classified as normal	Classified as tumour	Classified as both	Classified as None
Normal (40)	20	0	18	2
Tumour (40)	1	13	22	4

Table 20: Jack-knifing technique results of SIMCA where 40 matched pair cases were classified as normal, tumour, both normal and tumour, or neither.

The jack-knifing technique showed weak results, with specificity and sensitivity of 50% and about 33% respectively. 45% of normal cases and 55% of tumour cases were classified under both normal and tumour PCA models due to the overlap between normal and tumour. 2 normal and 4 tumour cases were classified as neither normal nor tumour.

Jack-knifing was then repeated on all samples using a model of only 29 samples. The selection of these samples was based on excluding the samples clustering in the central region from the models. Figure 23 below shows the model that has been used in the prediction of samples as described in table 13 and 14.

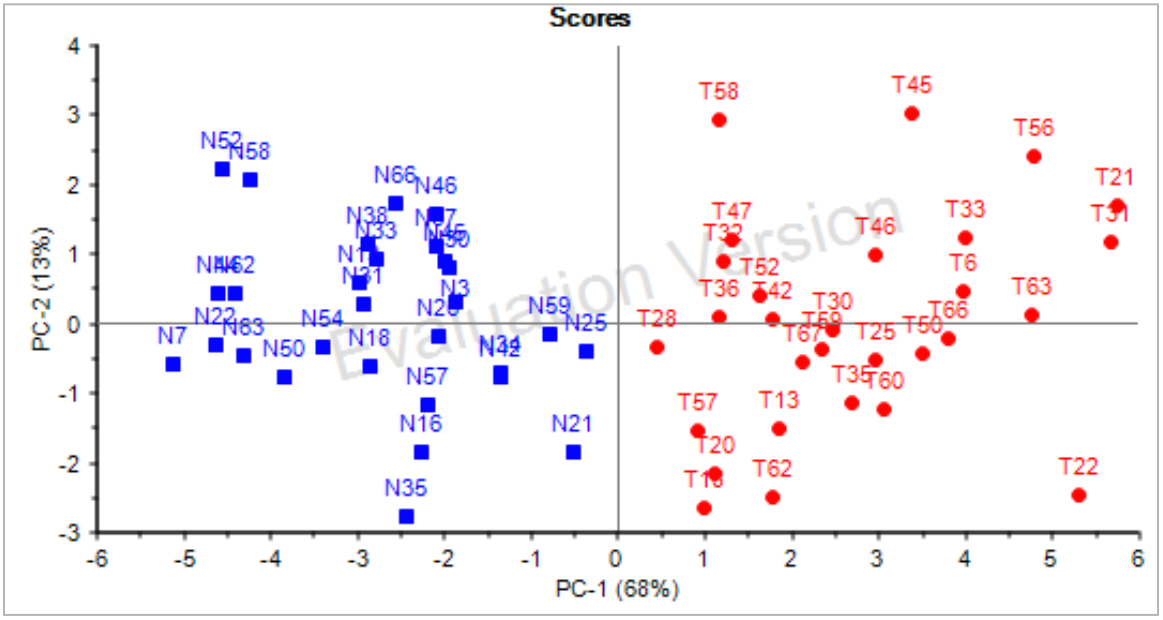

Figure 23: PCA model of 29 normal and 29 tumour samples used in the classification.

This classification also used the same statistically significant variables as discussed above. The models were then used to predict the tissue classification of all 40 samples. Table 21 displays classification results using this technique.

	Classified as normal	Classified as tumour	Classified as both	Classified as None
Normal (40)	24	3	10	3
Tumour (40)	1	21	14	4

Table 21: Results from classification technique where 29 samples were used for model construction to predict all 40 samples. Samples were classified as normal, tumour, both or neither.

This technique resulted in stronger predictive results where specificity was 60% and sensitivity was just above 50%. This showed slight improvement from the above results of specificity of 50% and sensitivity of about 33% respectively, as shown in table 20.

The above model was used to predict only the 29 samples. The results are summarized below in table 22.

	Classified as normal	Classified as tumour	Classified as both	Classified as None
Normal (29)	24	0	3	2
Tumour (29)	1	20	5	3

Table 22: Results from classification technique where 29 samples were used in construction of the PCA models. Samples were classified as normal, tumour, both or neither.

This technique resulted in more promising results where specificity was over 80% and sensitivity was about 70%. Only 3 normal and 5 tumours were classified as both and 2 normal and 3 tumours were classified as neither normal nor tumour.

One of the major limitations of the modeling is that the histological analysis was conducted on the entire sample, whereas the optical measurements were only performed on a tissue size of 2 mm, limited by the probe diameter. Therefore the histological analysis provided fat and tumour content on the entire sample, whereas only a small section of the sample was measured. A more accurate technique would be to perform histological analysis only on the measured area of the tissue by cutting or excising out the area measured. This would refine the fat and tumour content to the actual measured area.

Chapter 6: Discussion and Conclusion

6.1 Fluorescence Lifetime

Numerous studies (Kauppila et al., 1998, Deak et al., 1991) have reported that collagen type I has a significantly higher lifetime (3.2 ns) than collagen type III, and IV. However, collagen type II has been reported to have lifetime of 10 ns at 355 nm excitation (Coda et al., 2014). There has been a range of values for collagen fluorescence and lifetime in the literature. However, the complexity of collagen fluorescence makes it harder to differentiate between collagen types I, II, and III in the 390-410 nm range. Although classification of different collagen types is difficult, most studies have reported higher collagen fibrils and thus longer collagen lifetimes in diseased states in comparison to healthy states, verifying our results of significantly higher tumour lifetime (4.3 ns) compared to normal collagen at (3.5 ns) at the wavelength of 400 nm corresponding to collagen emission, as shown in table 12 and figure 14.

NADH has a peak emission wavelength of 460 nm upon 355 nm excitation and a mean fluorescence lifetime ranging from 0.2-0.4 ns in its free state. However, when NADH is protein bound, it will exhibit longer lifetimes typically in the ~2.5-3.4 ns range. Our measured response at 460 nm was 6.3 and 5.1 nm for normal and tumour breast tissue respectively, higher than the reported protein bound NADH lifetime. One study compared free state and protein bound NADH content and reported significantly decreased ($p<0.05$) protein-bound NADH in tumourous tissue compared to normal tissue. This change was attributed to a shift in metabolic conditions from oxidative phosphorylation to glycolysis, which is consistent with the predictions of tumour metabolism (Skala et al., 2007). Less

protein-bound NADH results in an overall quicker lifetime for the diseased state as observed in our results in table 12 and figure 14.

Our results showed lower FAD lifetime in tumour of 5.2 ns compared to the normal 7.1 ns breast samples, which falls within the range of published data as free state FAD has been reported to have a decay time of 5 ns, with a faster lifetime of about 1 ns in the bound form (Pires et al., 2014). Any changes in the NADH/FAD and their relative amounts of free and protein-bound states depend on the glycolysis and oxidative phosphorylation ratio. Since tumour progression results in a shift from oxidative phosphorylation to glycolysis, comparing short and long lifetime fluorescence decays of NADH and FAD can be used to discriminate between different metabolic conditions. Hence, NADH and FAD are biological molecules that could be used as biomarkers to reveal information on tumour metabolism (Pires et al., 2014).

6.2 Fluorescence Intensity

The increase of collagen deposition in malignant breast tissue has been observed in many previous studies (Kauppila et al., 1998, Fang et al., 2014, Provenzano et al., 2008, Haka et al., 2005, Zhu et al., 2008, Luparello et al., 1988). Collagen type I is a major constituent of the dermis and is found to reside primarily in the fibrous stroma of breast tissue whereas breast tissue high in adipose levels were found to have significantly lower collagen composition (Zhu et al., 2008). Other ex-vivo studies reported an over-deposition of collagen bundles of type I and III fibrils at tumour sites (Fang et al., 2014). Collagen type V was also present in about 10% of total collagen in tumourous breasts, whereas only 1% of total collagen in normal breast is type V collagen (Luparello et al., 1988). In normal breast tissue, collagen surrounding epithelial structures is smooth and

curly in structure, however, with tumour progression, the collagen thickens, linearizes and stiffens, promoting metastasis and promoting cells migration into the extra cellular matrix (ECM). Many studies have confirmed that increased density in breast correlates to higher incidences of breast cancers. This increase in breast density can be attributed to increased fibril collagen deposition and thus collagen can be hypothesized to promote tumorigenesis. Provenzano et al. (2008) demonstrated that tumour formation, invasion and metastasis in breast tissue are enhanced in collagen-dense stroma (Provenzano et al., 2008). Haka et al. concluded increased collagen in both benign and cancerous breast tissue relative to normal breast tissue using Raman spectroscopy (Haka et al., 2006). All previous literature matches our results of significantly increased collagen content (amplitude of 0.572 a.u. and integral area of 15.778 a.u.) at 400 nm in tumour compared to the normal (amplitude of 0.368 a.u. and integral area of 9.746 a.u.) breast samples as per figure 15 and table 13.

Another major fluorescence component displaying significant differences between tumour and normal breast tissue at 460 nm is the emission of NADH. Like collagen, NADH is also found to be significantly higher in tumour compared to the normal breast samples. NADH is one of the main coenzymes responsible for metabolic activities and the relative concentration of this coenzyme changes according to the status of oxidative metabolism of the cells. NADH concentration can be monitored as the shift from oxidative phosphorylation to aerobic glycolysis is observed in the progression from normal to malignant state. In glycolysis, glucose is converted to two pyruvate molecules that are subsequently converted into lactate, resulting in a net production of 2 ATP and 2 NADH molecules whereas in oxidative phosphorylation, glucose results in 36 ATP

molecules and 10 NADH that are then oxidized to NAD+ molecules. Thus, the shift to glycolysis results in an increase in NADH (Ostrander et al., 2010). (Zhu et al., 2008, Xu et al., 2015, Skala et al., 2007, Uppal and Gupta, 2003, Pires et al., 2014) also found significantly higher NADH levels in malignant breast tissue and attributed the higher NADH levels to an imbalance in metabolic activity associated with increased proliferation of ducts and lobular secretion, compared to normal breast tissue where adipose tissue have a more stable metabolic rate (Zhu et al., 2008). Increased NADH in tumour compared to normal has also been noted by our study where tumour displayed higher NADH amplitude (0.986 a.u.) and integral area (62.517 a.u.) in comparison to normal NADH amplitude (0.971 a.u.) and integral area of (60.720 a.u.) as shown in table 14 and figure 15 which agrees with the above literature.

The third constituent of the emission spectra peaking at 510 nm in figure 15 is attributed to FAD. Like NADH, FAD is another coenzyme responsible for cellular metabolism. The high-energy demands and biomass cell production in breast cancer results in major metabolic reprogramming in tumour state, affecting the levels of FAD present within the cell. In normal conditions, NADH, acting as an electron donor, reduces FAD to $FADH_2$. After a series of intermediate reactions, $FADH_2$ then binds to molecular oxygen to become oxidized to FAD. However, in tumour development, the low oxygen concentrations prevent the conversion of $FADH_2$ to FAD, thereby resulting in lower levels of FAD in tumour breast compared to normal breast samples (Wojcieszynska et al., 2012). This explains the lower FAD content (amplitude of 0.258 a.u. and integral area of 9.935 a.u.) observed in the tumour breast tissue samples compared to the normal FAD

content (amplitude of 0.332 a.u. and integral area of 13.659 a.u.) reported in our study (table 15).

Although NADH and FAD values provide information on the metabolic state of the tissue, the ratio of NADH to FAD is a more accurate measurement as it provides a control for cell density and accounts for metabolic variation between a healthy and diseased cellular status. Since NADH is one of the main electron donors while FAD is an electron acceptor in cellular metabolism, the oxidation-reduction (red-ox) ratio is a more robust measure of cellular metabolism and can be determined by the ratio of NADH to FAD (Ostrander et al., 2010). This red-ox ratio is important to monitor, as it is sensitive to cellular metabolic changes and oxygen depletion occurring during the progression of healthy to malignant state. As discussed above, there is a shift in metabolic process from oxidative phosphorylation to glycolysis. In oxidative phosphorylation, NADH is oxidized to its NAD+ form. However, due to depletion of oxygen levels in the tumour state, there is a decrease in the oxidation of NADH to NAD+ resulting in an accumulation of NADH (Alhallak et al., 2016). In oxidative phosphorylation, there is also an increase in FADH conversion to FAD, resulting in increased FAD levels in normal cellular conditions. However, the lower oxygen concentrations result in lower FAD levels in diseased conditions. As observed in this study, the increased NADH and decreased FAD levels observed in tumour tissue results in significantly increased NADH/FAD (amplitude of 3.978 a.u. and integral area of 6.854 a.u.) red-ox levels compared to the normal NADH/FAD content (amplitude of 3.07 a.u. and integral area of 4.88 a.u.) as shown in table 16.

6.3 Diffuse Reflectance

Diffuse reflectance is used to reveal information on the absorption and scattering of the biological tissue. The absorption coefficient provides information on the main absorbers present such as oxygenated and de-oxygenated hemoglobin while the reduced scattering coefficient provides information on the scattering bodies within the tissue. In tumour tissue, increased cell nuclei, collagen fibers, cross-links in the stroma as well as organelles, results in increased backscatter, or diffuse reflectance output (Yu et al., 2014). This allows the use of diffuse reflectance as a quantitative tool that can exhibit changes in physiological and morphological changes in tumour tissue. Numerous studies have used diffuse reflectance as an individual modality to discriminate between diseased and healthy tissue (Bigio et al., 2000, Zhu et al., 2006b, Palmer et al., 2002, Volynskaya et al., 2008, Evers et al., 2013) and observed higher diffuse reflectance in tumour compared to normal breast tissue. Bigio et al., (2000) reported sensitivity of 69% and specificity of 85 % in an in-vivo study to differentiate between malignant and non malignant breast tissue, while Zhu et al., reported 83 % and 76% sensitivity and specificity respectively. However, Palmer et al., (2002) conducted ex-vivo studies on breast tissue and observed a lower sensitivity of 30% and 78% specificity using diffuse reflectance alone. This was consistent with our findings as shown in table 17 and figure 16 in section 5.2.3 where higher DR was noted for tumour samples (0.409 a.u at 545 nm and 0.395 a.u. at 575 nm) when compared to normal breast samples (0.312 a.u at 545 nm and 0.306 a.u. at 575 nm).

6.3.1 Absorption coefficient

Although no significant differences were observed between the average absorption coefficient in tumour and normal samples in our study as shown in section 5.2.4.1 (figure

17 and table 18), other studies found significantly higher absorption in normal compared to tumour tissue, especially at 545 and 575 nm, wavelengths corresponding to oxygenated hemoglobin, the main absorber present in breast tissue. Zhu et al., (2008) attributed the decrease in hemoglobin saturation in malignant breast tissue to the limited oxygen supply in the rapidly proliferating tumour cells. Zhu also noted significantly higher hemoglobin saturation in normal and benign tissue compared to malignant tumour.

6.3.2 Reduced scattering coefficient

The reduced scattering coefficient provides information on the scattering centers present in the biological tissue, such as the nuclei. Since increases in cellular proliferation and cell density is a hallmark of tumour progression, an increase in the reduced scattering coefficient is anticipated in tumour tissue. The reduced scattering coefficient was also shown to increase as a result of increased nuclear size, DNA content and hyperchromasia (Yu et al., 2014). Significantly higher reduced scattering coefficient was observed in tumour (22.162 cm^{-1} at 545 nm and 21.273 cm^{-1} at 575 nm) compared to the normal breast tissue (18.571 cm^{-1} at 545 nm and 17.826 cm^{-1} at 575 nm) as per table 19 and figure 18, which was consistent with findings from previous studies (Ghosh et al., 2001, Breslin et al., 2004, Glennie et al., 2014, Vishwanath et al., 2011). Zhu et al., (2008) noted that the reduced scatter coefficient was inversely correlated to the amount of adipose tissue present as well as the patient body mass index (BMI). The observed increase in the reduced scatter coefficient observed in this study could be linked to increased fibro-connective and glandular tissue content and thus cancer development. The reduced scattering coefficient was also found to be significantly higher in benign tumours when compared to normal tissue and significantly higher in malignant tumours compared to

benign tumour, showing the potential of the reduced scattering coefficient to not only differentiate between tumour and normal state, but a more refined classification of tumour class and the ability to use the reduced scattering coefficient as a valuable parameter in tissue classification.

6.4 Classifications and Prediction

PCA models were built and tested using SIMCA to predict the unknown samples. A normal and tumour model was constructed using 29 cases that yielded specificity of over 80% and sensitivity of about 70%. These models were used to predict all forty samples using the jack-knifing technique and yielded results of 60% specificity and sensitivity just above 50%. The constraints of the modeling outcomes are described in the following chapter.

6.5 Conclusion

The time-resolved fluorescence and diffuse reflectance spectroscopy system was used to discriminate between normal and tumour breast samples in 40 matches pair cases. The fluorescence intensity was used to provide information on the endogenous fluorophores collagen, NADH and FAD. The diffuse reflectance was used to reveal tissue optical properties; the absorption and reduced scatter coefficient. Histological analysis was performed on all tissues to specify the fat and tumour content within each of the normal and tumour samples respectively. Statistical significant variables (collagen, NADH, FAD, and NADH/FAD amplitude and integral area, as well as the diffuse reflectance spectra and the reduced scattering coefficient) were used along with histological tissue classifications in constructing the normal and tumour principle component models. SIMCA was used as a binary classification tool to predict tissue as either normal or

tumour using PC models and achieved sensitivity of 60% and specificity slightly above 50%.

6.6 Future work

Although the sensitivity and specificity were lower than expected, the accuracy of the models can be significantly improved with modifications applied to methodology, modeling and data analysis. This study looked at fluorescence and diffuse reflectance independently. However, since fluorescence spectroscopy is affected by absorption and scattering events in the biological tissue, future work can aim to look at the integration of the diffuse reflectance data to adjust and modify the fluorescence data for scattering and absorption events. This retrieval of the intrinsic fluorescence can significantly improve the accuracy of the tr-FRS system. Another adjustment is to accurately label or cut out the breast tissue after optical measurements at the exact measurement location to ensure histological analysis is being performed on the area of interest to reveal more precise tumour and fat content evaluation. Another technique to resolve this issue could be to conduct more repeat measurements on a single specimen, so that the average fluorescence lifetime, fluorescence intensity, and diffuse reflectance would better represent the whole tissue. Our current histological analysis was conducted on bulk tissue and any tissue inhomogenieties may have resulted in imprecise quantification of tissue fat and tumour content. Furthermore, previous work has looked at calculating ß-carotene and hemoglobin concentration calculations to assist in differentiating between normal and malignant breast tissue. An addition to our modeling would be including ß-carotene and hemoglobin concentration calculations extracted from the optical properties using Monte Carlo

simulations and could display significant differences between tumour and normal breast samples as well as potentially strengthening modeling, prediction and classification.

References

ALFANO, R. R., TANG, G. C., PRADHAN, A., LAM, W., CHOY, D. S. J. & OPHER, E. 1987. FLUORESCENCE-SPECTRA FROM CANCEROUS AND NORMAL HUMAN-BREAST AND LUNG TISSUES. *Ieee Journal of Quantum Electronics,* 23**,** 1806-1811.

ALFANO, R. R., TATA, D. B., CORDERO, J., TOMASHEFSKY, P., LONGO, F. W. & ALFANO, M. A. 1984. LASER-INDUCED FLUORESCENCE SPECTROSCOPY FROM NATIVE CANCEROUS AND NORMAL TISSUE. *Ieee Journal of Quantum Electronics,* 20**,** 1507-1511.

ALHALLAK, K., REBELLO, L. G., MULDOON, T. J., QUINN, K. P. & RAJARAM, N. 2016. Optical redox ratio identifies metastatic potential-dependent changes in breast cancer cell metabolism. *Biomedical Optics Express,* 7**,** 4364-4374.

BEREZIN, M. Y. & ACHILEFU, S. 2010. Fluorescence Lifetime Measurements and Biological Imaging. *Chemical Reviews,* 110**,** 2641-2684.

BIGIO, I. J., BOWN, S. G., BRIGGS, G., KELLEY, C., LAKHANI, S., PICKARD, D., RIPLEY, P. M., ROSE, I. G. & SAUNDERS, C. 2000. Diagnosis of breast cancer using elastic-scattering spectroscopy: preliminary clinical results. *Journal of Biomedical Optics,* 5**,** 221-228.

BOPPART, S. A., LUO, W., MARKS, D. L. & SINGLETARY, K. W. 2004. Optical coherence tomography: feasibility for basic research and image-guided surgery of breast cancer. *Breast Cancer Research and Treatment,* 84**,** 85-97.

BRESLIN, T. M., XU, F. S., PALMER, G. M., ZHU, C. F., GILCHRIST, K. W. & RAMANUJAM, N. 2004. Autofluorescence and diffuse reflectance properties of malignant and benign breast tissues. *Annals of Surgical Oncology,* 11**,** 65-70.

CAPPON, D. J., FARRELL, T. J., FANG, Q. Y. & HAYWARD, J. E. 2013. Fiber-optic probe design and optical property recovery algorithm for optical biopsy of brain tissue. *Journal of Biomedical Optics,* 18.

CARNEY, P. A., MIGLIORETTI, D. L., YANKASKAS, B. C., KERLIKOWSKE, K., ROSENBERG, R. & RUTTER, C. M. 2003. Individual and combined effects of age, breast density, and hormone replacement therapy use on the accuracy of screening mammography (vol 138, pg 168, 2003). *Annals of Internal Medicine,* 138**,** 771-771.

CHOE, R. & IEEE. 2009. Diffuse Optical Tomography & Spectroscopy in Breast Cancer Characterization & Therapy Monitoring at UPENN. Annual International Conference of the IEEE-Engineering-in-Medicine-and-Biology-Society, Sep 03-06 2009 Minneapolis, MN. 6335-6337.

CHORVAT, D. & CHORVATOVA, A. 2009. Multi-wavelength fluorescence lifetime spectroscopy: a new approach to the study of endogenous fluorescence in living cells and tissues. *Laser Physics Letters,* 6**,** 175-193.

CODA, S., THOMPSON, A. J., KENNEDY, G. T., ROCHE, K. L., AYARU, L., BANSI, D. S., STAMP, G. W., THILLAINAYAGAM, A. V., FRENCH, P. M. W. & DUNSBY, C. 2014. Fluorescence lifetime spectroscopy of tissue autofluorescence in normal and diseased colon measured ex vivo using a fiber-optic probe. *Biomedical Optics Express,* 5**,** 515-538.

CROCE, A. C. & BOTTIROLI, G. 2014. Autofluorescence spectroscopy and imaging: a tool for biomedical research and diagnosis. *European Journal of Histochemistry,* 58**,** 320-337.

DE BEULE, P. A. A., DUNSBY, C., GALLETLY, N. P., STAMP, G. W., CHU, A. C., ANAND, U., ANAND, P., BENHAM, C. D., NAYLOR, A. & FRENCH, P. M. W. 2007. A hyperspectral fluorescence lifetime probe for skin cancer diagnosis. *Review of Scientific Instruments,* 78.

DEAK, S. B., GLAUG, M. R., PIERCE, R. A., BANCILA, E., AMENTA, P., MACKENZIE, J. W., GRECO, R. S. & BOYD, C. D. 1991. DESMOPLASIA IN BENIGN AND MALIGNANT BREAST DISEASE IS CHARACTERIZED BY ALTERATIONS IN LEVEL OF MESSENGER-RNAS CODING FOR TYPE-I AND TYPE-III PROCOLLAGEN. *Matrix,* 11**,** 252-258.

EVERS, D. J., NACHABE, R., PEETERS, M. J. V., VAN DER HAGE, J. A., OLDENBURG, H. S., RUTGERS, E. J., LUCASSEN, G. W., HENDRIKS, B. H. W., WESSELING, J. & RUERS, T. J. M. 2013. Diffuse reflectance spectroscopy: towards clinical application in breast cancer. *Breast Cancer Research and Treatment,* 137**,** 155-165.

FANG, M., YUAN, J. P., PENG, C. W. & LI, Y. 2014. Collagen as a double-edged sword in tumor progression. *Tumor Biology,* 35**,** 2871-2882.

GHOSH, N., MOHANTY, S. K., MAJUMDER, S. K. & GUPTA, P. K. 2001. Measurement of optical transport properties of normal and malignant human breast tissue. *Applied Optics,* 40**,** 176-184.

GLENNIE, D. L., HAYWARD, J. E., MCKEE, D. E. & FARRELL, T. J. 2014. Inexpensive diffuse reflectance spectroscopy system for measuring changes in tissue optical properties. *Journal of Biomedical Optics,* 19.

GUPTA, P. K., MAJUMDER, S. K. & UPPAL, A. 1997. Breast cancer diagnosis using N-2 laser excited autofluorescence spectroscopy. *Lasers in Surgery and Medicine,* 21**,** 417-422.

HAKA, A. S., SHAFER-PELTIER, K. E., FITZMAURICE, M., CROWE, J., DASARI, R. R. & FELD, M. S. 2005. Diagnosing breast cancer by using Raman spectroscopy. *Proceedings of the National Academy of Sciences of the United States of America,* 102**,** 12371-12376.

HAKA, A. S., VOLYNSKAYA, Z., GARDECKI, J. A., NAZEMI, J., LYONS, J., HICKS, D., FITZMAURICE, M., DASARI, R. R., CROWE, J. P. & FELD, M. S. 2006. In vivo margin assessment during partial mastectomy breast surgery using Raman spectroscopy. *Cancer Research,* 66**,** 3317-3322.

HEIJBLOM, M., PIRAS, D., BRINKHUIS, M., VAN HESPEN, J. C. G., VAN DEN ENGH, F. M., VAN DER SCHAAF, M., KLAASE, J. M., VAN LEEUWEN, T. G., STEENBERGEN, W. & MANOHAR, S. 2015. Photoacoustic image patterns of breast carcinoma and comparisons with Magnetic Resonance Imaging and vascular stained histopathology. *Scientific Reports,* 5.

IFTIMIA, N., MUJAT, M., HICKS, A., PATEL, A., BISS, D., FERGUSON, R. D., HAMMER, D. & IEEE. 2011. Image-guided Breast Biopsy with Optical Coherence Tomography. Conference on Lasers and Electro-Optics (CLEO), May 01-06 2011 Baltimore, MD.

JACQUES, S. L. 2013. Optical properties of biological tissues: a review. *Physics in Medicine and Biology,* 58**,** R37-R61.

JAYANTHI, J. L., SUBHASH, N., MANJU, S., NISHA, U. G. & BEENA, V. T. 2012. Diffuse reflectance imaging: a tool for guided biopsy. Conference on Optical Biopsy X/SPIE Photonics West BiOS Conference, Jan 24-25 2012 San Francisco, CA. BELLINGHAM: Spie-Int Soc Optical Engineering.

KAUPPILA, S., STENBACK, F., RISTELI, J., JUKKOLA, A. & RISTELI, L. 1998. Aberrant type I and type III collagen gene expression in human breast cancer in vivo. *Journal of Pathology,* 186**,** 262-268.

KONG, K., KENDALL, C., STONE, N. & NOTINGHER, I. 2015. Raman spectroscopy for medical diagnostics - From in-vitro biofluid assays to in-vivo cancer detection. *Advanced Drug Delivery Reviews,* 89**,** 121-134.

KUHL, C. K., SCHRADING, S., LEUTNER, C. C., MORAKKABATI-SPITZ, N., WARDELMANN, E., FIMMERS, R., KUHN, W. & SCHILD, H. H. 2005. Mammography, breast ultrasound, and magnetic resonance imaging for surveillance of women at high familial risk for breast cancer. *Journal of Clinical Oncology,* 23**,** 8469-8476.

LI, X. Q., HELDERMON, C. D., YAO, L., XI, L. & JIANG, H. B. 2015. High resolution functional photoacoustic tomography of breast cancer. *Medical Physics,* 42**,** 5321-5328.

LUPARELLO, C., RIZZO, C. P., SCHILLACI, R. & PUCCIMINAFRA, I. 1988. FRACTIONATION OF TYPE-V COLLAGEN FROM CARCINOMATOUS AND DYSPLASIC BREAST IN THE PRESENCE OF ALKALINE POTASSIUM-CHLORIDE. *Analytical Biochemistry,* 169**,** 26-32.

MOHAMMAD MEHRMOHAMMADI , 2, * SOON JOON YOON , 1 DOUGLAS YEAGER , 1 AND STANISLAV Y. EMELIANOV 1, * 2013. Photoacoustic Imaging for Cancer Detection and Staging. Current Molecular Imaging.

MOURANT, J. R., BIGIO, I. J., BOYER, J., CONN, R. L., JOHNSON, T. & SHIMADA, T. 1995. Spectroscopic diagnosis of bladder cancer with elastic light scattering. *Lasers in Surgery and Medicine,* 17**,** 350-357.

MOURANT, J. R., BIGIO, I. J., BOYER, J. D., JOHNSON, T. M., LACEY, J., BOHORFOUSH III, A. G. & MELLOW, M. H. 1996. Elastic scattering spectroscopy as a diagnostic tool for differentiating pathologies in the gastrointestinal tract: preliminary testing. *Journal of biomedical optics,* 1**,** 192-9.

NGUYEN, F. T., ZYSK, A. M., CHANEY, E. J., KOTYNEK, J. G., OLIPHANT, U. J., BELLAFIORE, F. J., ROWLAND, K. M., JOHNSON, P. A. & BOPPART, S. A. 2009. Intraoperative Evaluation of Breast Tumor Margins with Optical Coherence Tomography. *Cancer Research,* 69**,** 8790-8796.

NIE, Z. J., AN, R., HAYWARD, J. E., FARRELL, T. J. & FANG, Q. Y. 2013. Hyperspectral fluorescence lifetime imaging for optical biopsy. *Journal of Biomedical Optics,* 18.

NIE, Z. J., DU LE, V. N., CAPPON, D., PROVIAS, J., MURTY, N., HAYWARD, J. E., FARRELL, T. J., PATTERSON, M. S., MCMILLAN, W. & FANG, Q. Y. 2016. Integrated Time-Resolved Fluorescence and Diffuse Reflectance Spectroscopy Instrument for Intraoperative Detection of Brain Tumor Margin. *Ieee Journal of Selected Topics in Quantum Electronics,* 22.

OSTRANDER, J. H., MCMAHON, C. M., LEM, S., MILLON, S. R., BROWN, J. Q., SEEWALDT, V. L. & RAMANUJAM, N. 2010. Optical Redox Ratio Differentiates Breast Cancer Cell Lines Based on Estrogen Receptor Status. *Cancer Research,* 70**,** 4759-4766.

PALMER, G. M., MARSHEK, C. L., VROTSOS, K. M. & RAMANUJAM, N. 2002. Optimal methods for fluorescence and diffuse reflectance measurements of tissue biopsy samples. *Lasers in Surgery and Medicine,* 30**,** 191-200.

PALMER, G. M., ZHU, C. F., BRESLIN, T. M., XU, F. S., GILCHRIST, K. W. & RAMANUJAM, N. 2003. Comparison of multiexcitation fluorescence and diffuse reflectance spectroscopy for the diagnosis of breast cancer (March 2003). *Ieee Transactions on Biomedical Engineering,* 50**,** 1233-1242.

PAPAIOANNOU, T., PREYER, N. W., FANG, Q. Y., BRIGHTWELL, A., CARNOHAN, M., COTTONE, G., ROSS, R., JONES, L. R. & MARCU, L. 2004. Effects of fiber-optic probe design and probe-to-target distance on diffuse reflectance measurements of turbid media: an experimental and computational study at 337 nm. *Applied Optics,* 43**,** 2846-2860.

PIRES, L., NOGUEIRA, M. S., PRATAVIEIRA, S., MORIYAMA, L. T. & KURACHI, C. 2014. Time-resolved fluorescence lifetime for cutaneous melanoma detection. *Biomedical Optics Express,* 5**,** 3080-3089.

PROVENZANO, P. P., INMAN, D. R., ELICEIRI, K. W., KNITTEL, J. G., YAN, L., RUEDEN, C. T., WHITE, J. G. & KEELY, P. J. 2008. Collagen density promotes mammary tumor initiation and progression. *Bmc Medicine,* 6.

PU, Y., TANG, G., DAS, B. B., LIU, C. H., PRADHAN, A. & ALFANO, R. R. 2012. Ultrafast time-dependent fluorescence spectroscopy for human breast cancer detection. Conference on Optical Biopsy X/SPIE Photonics West BiOS Conference, 2012

Jan 24-25 2012 San Francisco, CA.

RAJARAM, N., NGUYEN, T. H. & TUNNELL, J. W. 2008. Lookup table-based inverse model for determining optical properties of turbid media. *Journal of Biomedical Optics,* 13.

RAMANUJAM, N. 2000. Fluorescence spectroscopy of neoplastic and non-neoplastic tissues. *Neoplasia,* 2**,** 89-117.

REQUEJO-ISIDRO, J., MCGINTY, J., MUNRO, I., ELSON, D. S., GALLETLY, N. P., LEVER, M. J., NEIL, M. A. A., STAMP, G. W. H., FRENCH, P. M. W., KELLETT, P. A., HARES, J. D. & DYMOKE-BRADSHAW, A. K. L. 2004. High-speed wide-field time-gated endoscopic fluorescence-lifetime imaging. *Optics Letters,* 29**,** 2249-2251.

SHRESTHA, S., APPLEGATE, B. E., PARK, J., XIAO, X., PANDE, P. & JO, J. A. 2010. High-speed multispectral fluorescence lifetime imaging implementation for in vivo applications. *Optics Letters,* 35**,** 2558-2560.

SKALA, M. C., RICHING, K. M., BIRD, D. K., GENDRON-FITZPATRICK, A., EICKHOFF, J., ELICEIRI, K. W., KEELY, P. J. & RAMANUJAM, N. 2007. In vivo multiphoton fluorescence lifetime imaging of protein-bound and free nicotinamide adenine dinucleotide in normal and precancerous epithelia. *Journal of Biomedical Optics,* 12.

STATISTICS., C. C. S. S. A. C. O. C. 2015. Breast cancer statistics.

SUN, Y., HATAMI, N., YEE, M., PHIPPS, J., ELSON, D. S., GORIN, F., SCHROT, R. J. & MARCU, L. 2010. Fluorescence lifetime imaging microscopy for brain tumor image-guided surgery. *Journal of Biomedical Optics,* 15.

SZARKO, M., MULDREW, K. & BERTRAM, J. E. A. 2010. Freeze-thaw treatment effects on the dynamic mechanical properties of articular cartilage. *Bmc Musculoskeletal Disorders,* 11.

TADROUS, P. J., SIEGEL, J., FRENCH, P. M. W., SHOUSHA, S., LALANI, E. N. & STAMP, G. W. H. 2003. Fluorescence lifetime imaging of unstained tissues: early results in human breast cancer. *Journal of Pathology,* 199**,** 309-317.

UPPAL, A. & GUPTA, P. K. 2003. Measurement of NADH concentration in normal and malignant human tissues from breast and oral cavity. *Biotechnology and Applied Biochemistry,* 37**,** 45-50.

VAN DE VEN, S., ELIAS, S., WIETHOFF, A., VAN DER VOORT, M., LEPROUX, A., NIELSEN, T., BRENDEL, B., BAKKER, L., VAN DER MARK, M., MALI, W. & LUIJTEN, P. 2009. Diffuse Optical Tomography of the Breast: Initial Validation in Benign Cysts. *Molecular Imaging and Biology,* 11**,** 64-70.

VISHWANATH, K., CHANG, K., KLEIN, D., DENG, Y. F., CHANG, V., PHELPS, J. E. & RAMANUJAM, N. 2011. Portable, Fiber-Based, Diffuse Reflection Spectroscopy (DRS) Systems for Estimating Tissue Optical Properties. *Applied Spectroscopy,* 65**,** 206-215.

VOLYNSKAYA, Z., HAKA, A. S., BECHTEL, K. L., FITZMAURICE, M., SHENK, R., WANG, N., NAZEMI, J., DASARI, R. R. & FELD, M. S. 2008. Diagnosing breast cancer using diffuse reflectance spectroscopy and intrinsic fluorescence spectroscopy. *Journal of Biomedical Optics,* 13.

WEHRY, E. L. 1984. PRINCIPLES OF FLUORESCENCE SPECTROSCOPY - LAKOWICZ,JR. *American Scientist,* 72**,** 395-396.

WOJCIESZYNSKA, D., HUPERT-KOCUREK, K. & GUZIK, U. 2012. Flavin-Dependent Enzymes in Cancer Prevention. *International Journal of Molecular Sciences,* 13**,** 16751-16768.

XU, H. N., TCHOU, J., FENG, M., ZHAO, H. Q. & LI, L. Z. 2015. Differentiating cancerous from normal breast tissue by redox imaging. Conference on Photonic Therapeutics and Diagnostics XI, Feb 07-08 2015 San Francisco, CA. BELLINGHAM: Spie-Int Soc Optical Engineering.

YANG, Y. L., KATZ, A., CELMER, E. J., ZURAWSKASZCZEPANIAK, M. Z. & ALFANO, R. R. 1997. Fundamental differences of excitation spectrum between malignant and benign breast tissues. *Photochemistry and Photobiology,* 66**,** 518-522.

YU, B., SHAH, A., NAGARAJAN, V. K. & FERRIS, D. G. 2014. Diffuse reflectance spectroscopy of epithelial tissue with a smart fiber-optic probe. *Biomedical Optics Express,* 5**,** 675-689.

YUAN, Y., HWANG, J.-Y., KRISHNAMOORTHY, M., YE, K., ZHANG, Y., NING, J., WANG, R. C., DEEN, M. J. & FANG, Q. 2009. High-throughput acousto-optic-tunable-filter-based time-resolved fluorescence spectrometer for optical biopsy. *Optics Letters,* 34**,** 1132-1134.

ZHOU, Y. Z., LIU, C. H., LI, J. Y., LI, Z. W., ZHOU, L. X., CHEN, K., PU, Y., HE, Y., ZHU, K., LI, Q. B. & ALFANO, R. R. 2014. Tumor margin detection using optical biopsy techniques. Conference on Optical Biopsy XII, Feb 04-05 2014 San Francisco, CA. BELLINGHAM: Spie-Int Soc Optical Engineering.

ZHU, C., PALMER, G. M., BRESLIN, T. M., HARTER, J. & RAMANUJAM, N. 2006a. Diagnosis of breast cancer using diffuse reflectance spectroscopy: Comparison of a Monte Carlo versus partial least squares analysis based feature extraction technique. *Lasers in Surgery and Medicine,* 38**,** 714-724.

ZHU, C. F., PALMER, G. M., BRESLIN, T. M., HARTER, J. & RAMANUJAM, N. 2006b. Diagnosis of breast cancer using diffuse reflectance spectroscopy: Comparison of a Monte Carlo versus partial least squares analysis based feature extraction technique. *Lasers in Surgery and Medicine,* 38**,** 714-724.

ZHU, C. F., PALMER, G. M., BRESLIN, T. M., HARTER, J. & RAMANUJAM, N. 2008. Diagnosis of breast cancer using fluorescence and diffuse reflectance spectroscopy: a Monte-Carlo-model-based approach. *Journal of Biomedical Optics,* 13.

ZYSK, A. M. & BOPPART, S. A. 2006. Computational methods for analysis of human breast tumor tissue in optical coherence tomography images. *Journal of Biomedical Optics,* 11.